

## Yet anOther Dose Algorithm (YODA) for independent computations of dose and dose changes due to anatomical changes

Burlacu, Tiberiu; Lathouwers, Danny; Perko, Zoltan

**DOI**

[10.1088/1361-6560/ad6373](https://doi.org/10.1088/1361-6560/ad6373)

**Publication date**

2024

**Document Version**

Final published version

**Published in**

Physics in medicine and biology

**Citation (APA)**

Burlacu, T., Lathouwers, D., & Perko, Z. (2024). Yet anOther Dose Algorithm (YODA) for independent computations of dose and dose changes due to anatomical changes. *Physics in medicine and biology*, 69(16), Article 165003. <https://doi.org/10.1088/1361-6560/ad6373>

**Important note**

To cite this publication, please use the final published version (if applicable). Please check the document version above.

**Copyright**

Other than for strictly personal use, it is not permitted to download, forward or distribute the text or part of it, without the consent of the author(s) and/or copyright holder(s), unless the work is under an open content license such as Creative Commons.

**Takedown policy**

Please contact us and provide details if you believe this document breaches copyrights. We will remove access to the work immediately and investigate your claim.

PAPER • OPEN ACCESS

## Yet anOther Dose Algorithm (YODA) for independent computations of dose and dose changes due to anatomical changes

To cite this article: Tiberiu Burlacu *et al* 2024 *Phys. Med. Biol.* **69** 165003View the [article online](#) for updates and enhancements.

### You may also like

- [Anatomical robust optimization to account for nasal cavity filling variation during intensity-modulated proton therapy: a comparison with conventional and adaptive planning strategies](#)  
Steven van de Water, Francesca Albertini, Damien C Weber *et al.*
- [Holistic evaluation of a machine learning-based timing calibration for PET detectors under varying data sparsity](#)  
Stephan Naunheim, Florian Mueller, Vanessa Nadig *et al.*
- [Deep learning for intracranial aneurysm segmentation using CT angiography](#)  
Huizhong Zheng, Xinfeng Liu, Zhenxing Huang *et al.*



**Joining forces:**  
One complete  
QA solution for  
Dosimetry with  
myQA<sup>®</sup>, QUASAR<sup>™</sup>  
and Radcal<sup>®</sup>!





## PAPER

## OPEN ACCESS

RECEIVED  
2 April 2024REVISED  
26 June 2024ACCEPTED FOR PUBLICATION  
15 July 2024PUBLISHED  
30 July 2024

Original Content from  
this work may be used  
under the terms of the  
[Creative Commons  
Attribution 4.0 licence](#).

Any further distribution  
of this work must  
maintain attribution to  
the author(s) and the title  
of the work, journal  
citation and DOI.



# Yet anOther Dose Algorithm (YODA) for independent computations of dose and dose changes due to anatomical changes

Tiberiu Burlacu<sup>1,2,\*</sup> , Danny Lathouwers<sup>1,2,3</sup> and Zoltán Perkó<sup>1,2,3</sup> <sup>1</sup> Faculty of Applied Sciences, Delft University of Technology, Delft, The Netherlands<sup>2</sup> HollandPTC consortium—Erasmus Medical Center, Rotterdam, Holland Proton Therapy Centre, Delft, Leiden University Medical Center (LUMC), Leiden and Delft University of Technology, Delft, The Netherlands<sup>3</sup> Both authors contributed equally.

\* Author to whom any correspondence should be addressed.

E-mail: [t.burlacu@tudelft.nl](mailto:t.burlacu@tudelft.nl)**Keywords:** proton therapy, online adaptive, patient specific, quality assurance, anatomy changes

## Abstract

**Objective.** To assess the viability of a physics-based, deterministic and adjoint-capable algorithm for performing treatment planning system independent dose calculations and for computing dosimetric differences caused by anatomical changes. **Approach.** A semi-numerical approach is employed to solve two partial differential equations for the proton phase-space density which determines the deposited dose. Lateral heterogeneities are accounted for by an optimized (Gaussian) beam splitting scheme. Adjoint theory is applied to approximate the change in the deposited dose caused by a new underlying patient anatomy. **Main results.** The dose engine's accuracy was benchmarked through three-dimensional gamma index comparisons against Monte Carlo simulations done in TOPAS. For a lung test case, the worst passing rate with (1 mm, 1%, 10% dose cut-off) criteria is 94.55%. The effect of delivering treatment plans on repeat CTs was also tested. For non-robustly optimized plans the adjoint component was accurate to 5.7% while for a robustly optimized plan it was accurate to 4.8%. **Significance.** Yet anOther Dose Algorithm is capable of accurate dose computations in both single and multi spot irradiations when compared to TOPAS. Moreover, it is able to compute dosimetric differences due to anatomical changes with small to moderate errors thereby facilitating its use for patient-specific quality assurance in online adaptive proton therapy.

## 1. Introduction

### 1.1. Online adaptive proton therapy (OAPT) and quality assurance

Proton therapy (PT) promises to improve on conventional photon based radiotherapy for curative cancer treatments due to the characteristics of its dose-depth curve. The proton dose-depth curve shows simultaneously lower doses achievable in organs at risk (OARs) and an increased target dose conformality due to the presence of the Bragg peak (BP) (Paganetti 2016). Both target dose conformality and dose in OARs can however be degraded by the presence of uncertainties. Typical examples of uncertainty sources are the conversion of Hounsfield units (HU) in Computed Tomography (CT) scans to proton stopping powers, the daily positioning of the patient in the treatment room or the short and long-term anatomical changes occurring in the patient (Lomax 2008a, 2008b). To improve target coverage, clinical proton plans are subjected to robust optimization (der Voort *et al* 2016). Robust optimization seeks to create plans that perform well under a number of error scenarios such as range and patient set-up errors (Unkelbach and Paganetti 2018). In doing so, robust optimization creates a high dose margin around the target in the surrounding OARs (Van de Water *et al* 2016). While this makes treatments less sensitive to the included range and setup errors, other scenarios (e.g. weight loss over the course of week long treatments) are too complex to be modelled in a straightforward manner (Paganetti *et al* 2021).

The workflow of OAPT would allow the reduction of the complexity and number of robust optimization scenarios. In this workflow, a new daily CT scan of the patient is acquired, a new fully re-optimized treatment plan is quickly created and thereafter safely delivered (Botas *et al* 2018). This workflow would avoid tumor underdosage and would result in a lowering of the Normal Tissue Complication Probability (NTCP) through the reduction of the necessary margins around the tumor down to the intra-fractional ones for a robustly optimized plan (Paganetti *et al* 2021). Unfortunately, the computational expense of plan re-optimization (Men *et al* 2010) and the time needed for the (mostly manual) plan quality assurance (QA) process (Barrett *et al* 2009) have so far rendered this workflow practically infeasible.

Machine QA (ranging from daily to yearly) procedures entail a series of time-consuming measurements meant to assess the constancy of beam properties and the correct functioning of its delivery system (Arjomandy *et al* 2009, Li *et al* 2013). In addition patient-specific quality assurance (PSQA) must also be performed, with the goal to assess whether the differences between the planned and delivered dose distributions are within the clinically acceptable range of  $\pm 3\%$  (Gottschalk 2004) and to perform an independent check of the patient-specific dose that the treatment planning system (TPS) computes (Johnson *et al* 2019). Additionally, PSQA also functions as a redundant check of the machine function (Frank and Zhu 2020). Currently, PSQA is manually performed via dosimetric measurements which are infeasible in an OAPT workflow. TPS independent dose calculations (IDCs) based on log-files (records of the delivered spot positions and corresponding Monitor Units (MUs)) have been proposed as a solution for automating PSQA (Li *et al* 2013). They have been shown to have similar accuracy to dosimetric measurements and could yield clinically relevant metrics (Meier *et al* 2015, Meijers *et al* 2020). Such an approach has potential within the time-constrained workflow of OAPT and could also increase clinical throughput (Meijers *et al* 2020) by reducing the time spent on QA.

### 1.2. A hybrid independent dose computation approach

To perform fast, TPS independent and log-file based dose computations the interactions between the proton beam and the patient must be modelled, ideally not only using a different implementation of the TPS dose engine but using a different methodology altogether. The two methods that are likely to be employed by a TPS are the Monte Carlo (MC) method and the analytical PB method. The MC method (e.g. TOPAS (Perl *et al* 2012)) trades fast computation times for high computational precision (Zheng-Ming and Brahme 1993) by solving the in-tissue proton balance equation (i.e. the Linear Boltzmann equation) using statistical sampling methods. The analytical PB method (e.g. Bortfeld's model (Bortfeld 1997)) trades high precision for fast computation times by employing a series of approximations and fits to obtain the dose in the tissue of interest. PB methods are still routinely used in TPS (Trnková *et al* 2016) despite their limitations being well documented (Soukup *et al* 2005).

We previously presented a methodologically different approach based on a deterministic solution of the Linear Boltzmann equation (Burlacu *et al* 2023). This approach, which will henceforth be referred to as Yet anOther Dose Algorithm (YODA), is a hybrid numerical and analytical solution to a physics motivated approximation of the same equation that MC methods solve. The method strikes a balance in terms of accuracy versus speed. It is accurate with respect to MC methods due to the physical modelling of the interactions between the proton beam and the patient and it is fast due to the partly analytical solution. An additional advantage of this approach is the ease of applying the adjoint method. Given planning and repeat CT images with delineated structures and a treatment plan the adjoint method computes an approximation of the change in dose caused by delivering the treatment plan to the repeat CT image, thereby avoiding an expensive re-computation. Such an approximation could be used for triggering a plan adaptation on the given day.

The purpose of this work is to demonstrate and test YODA's performance in real anatomies. Thus, YODA is compared to TOPAS, disregarding nuclear interactions, in several irradiation sites. Moreover, the adjoint engine's capability of accurately computing dose changes due to anatomy changes is benchmarked using TPS generated irradiation plans. This paper also documents the improvements brought to YODA, i.e. a more stable and an order more accurate numerical integration method, a better elastic scattering model for the proton beam, improved modelling in the Fermi-Eyges (FE) equation, a laterally optimized Gaussian beam splitting scheme and RT DICOM clinical treatment plan reading, compared to the original documented version (Burlacu *et al* 2023). The details of these changes next to the theoretical framework of YODA are given in section 2. Section 3 presents the results and their discussion while section 4 presents the conclusions and future outlook.

## 2. Methods

### 2.1. Algorithm components

To model the 6-dimensional proton phase-space density in the patient the integro-differential Linear Boltzmann equation, which all MC methods are based on, is simplified using physics based approximations. The approximations employed, namely the continuous slowing down approximation, the energy-loss straggling approximation, the small-angle Fokker–Planck (FP) approximation, together with the separation of the proton phase-space density (Gebäck and Asadzadeh 2012) into

$$\varphi(\mathbf{r}, \hat{\Omega}, E) = \varphi_{FE}(\mathbf{r}, \hat{\Omega}) \cdot \varphi_{FP}(z, E), \quad (1)$$

results in two partial differential equations (PDEs) that describe the proton phase-space density in an in-depth heterogeneous and laterally homogeneous geometry. The first PDE is the one-dimensional FP equation (Pomraning 1996),

$$1DFP(\varphi_{FP}) = \frac{\partial \varphi_{FP}}{\partial z} - \frac{\partial S(z, E) \varphi_{FP}}{\partial E} - \frac{1}{2} \frac{\partial^2 T(z, E) \varphi_{FP}}{\partial E^2} + \Sigma_a(z, E) \varphi_{FP} = 0, \quad (2)$$

with  $\varphi_{FP} = \varphi_{FP}(z, E)$  the proton FP flux that depends on the depth along the central axis of the beam  $z \in \mathbb{R}$  and on the beam energy  $E \in \mathbb{R}$ ,  $S(z, E)$  the proton stopping power,  $T(z, E)$  the energy straggling coefficient and  $\Sigma_a(z, E)$  the macroscopic absorption cross section. The second equation is the FE equation (Eyges 1948, Pomraning and Prinja 1999),

$$\Upsilon(\varphi_{FE}) = \frac{\partial \varphi_{FE}}{\partial z} + \Omega_x \frac{\partial \varphi_{FE}}{\partial x} + \Omega_y \frac{\partial \varphi_{FE}}{\partial y} - \frac{\overline{\Sigma}_{tr}(z)}{2} \left( \frac{\partial^2 \varphi_{FE}}{\partial \Omega_x^2} + \frac{\partial^2 \varphi_{FE}}{\partial \Omega_y^2} \right) = 0, \quad (3)$$

with  $\varphi_{FE} = \varphi_{FE}(\hat{\Omega}, \mathbf{r})$  the FE flux,  $\hat{\Omega} = (\Omega_x, \Omega_y) \in \mathbb{R}^2$  the direction cosines along the  $x$  and  $y$  proton velocity axes,  $\mathbf{r} = (x, y, z) \in \mathbb{R}^3$  a point in physical beam-eye view space (with  $z$  the depth along the beam) and  $\overline{\Sigma}_{tr}(z)$  the energy spectrum (i.e.  $\varphi_{FP}$ ) averaged macroscopic transport cross section.

By solving equations (2) and (3) the 6-dimensional proton phase-space density  $\varphi$  is obtained, which in turn yields all clinically relevant metrics, such as the dose distribution or the NTCP.

#### 2.1.1. The FP equation

The one-dimensional FP equation (2) is numerically solved using the Symmetric Interior Penalty Galerkin (SIPG) (Rivière 2008) method in the energy domain and the three-stage, third-order accurate Singly Diagonally Implicit Runge-Kutta (SDIRK) method (Kennedy and Carpenter 2016) in space (depth). The energy domain is discretized into  $N_g$  intervals called groups. Within each group  $\varphi_{FP}$  is approximated as an expansion around the first three group-centered Legendre polynomial basis functions resulting in a method that is third order accurate in energy. The one-dimensional FP equation (2) is supplemented with global boundary conditions in energy (BCE) and space (BCS),

$$\text{BCE: } \varphi_{FP}(z, E) \Big|_{E=E_{\max}} = 0, \quad \frac{\partial \varphi_{FP}(z, E)}{\partial E} \Big|_{E=E_{\max}} = 0, \quad \frac{\partial \varphi_{FP}(z, E)}{\partial E} \Big|_{E=E_{\min}} = 0, \quad (4)$$

$$\text{BCS: } \varphi_{FP}(0, E) = A e^{-\left(\frac{E-E_0}{\sigma_E}\right)^2}, \quad (5)$$

to ensure a unique solution. The energy boundary conditions are of the Dirichlet and Neumann type, while the space boundary condition is a Gaussian function with amplitude  $A$ , nominal beam energy  $E_0$  and spread  $\sigma_E$ . Gerbershagen *et al* (2017) showed that this is a realistic energy spectrum for protons that underwent energy degradation. After discretizing the system in energy a so called semi-discrete system of equations is obtained that is thereafter solved using the SDIRK3 method<sup>3</sup>.

#### 2.1.2. The FE equation

The advantage of the FE equation (3) is its analytical solution via Fourier transforms (Gebäck and Asadzadeh 2012), namely

$$\varphi_{FE}(z, \boldsymbol{\rho}, \hat{\Omega}) = \frac{A^2}{4\pi^2} \frac{\exp\left(-\frac{|\boldsymbol{\rho}|^2}{2\bar{\xi}^2(z)}\right) \exp\left(-\frac{1}{2B(z)} \left| \hat{\Omega} - \frac{\overline{\theta\xi}(z)}{\bar{\xi}^2(z)} \boldsymbol{\rho} \right|^2\right)}{\bar{\xi}^2(z) B(z)}. \quad (6)$$

<sup>3</sup> When compared to the Crank–Nicholson method in our earlier work (Burlacu *et al* 2023), this method increased the accuracy of the FP fluxes without degrading the speed of the algorithm.

The solution from equation (6) is a Gaussian in the beam lateral coordinates  $\boldsymbol{\rho} = (x, y)$  and in the angular coordinates  $\hat{\boldsymbol{\Omega}} = (\Omega_x, \Omega_y)$  with its depth-dependent FE coefficients, namely  $\overline{\theta^2}(z)$  (variance of the angular direction),  $\overline{\xi^2}(z)$  (variance of the lateral position),  $\overline{\theta\xi}(z)$  (covariance of the lateral position and angular direction) (Gottschalk 2012), determined by the material path encountered along the central axis of the beam. The solution  $\varphi_{\text{FE}}$  is obtained by imposing a boundary condition that is a product of two identical double Gaussians, one in  $(x, \Omega_x)$  and one in  $(y, \Omega_y)$ .

As shown in section 2.2, to obtain the dose in a physical region only the  $\overline{\xi^2}$  coefficient is needed. This is the second moment of  $\overline{\Sigma_{\text{tr}}}$  and is computed as

$$\overline{\xi^2}(z) = \overline{\xi^2}(0) + 2\overline{\theta\xi}(0)z + \overline{\theta^2}(0)z^2 + \int_0^z (z-z')^2 \overline{\Sigma_{\text{tr}}}(z') dz' \quad (7)$$

with  $\overline{\xi^2}(0)$ ,  $\overline{\theta^2}(0)$  and  $\overline{\theta\xi}(0)$  constants based on the imposed double Gaussian boundary condition. The quantity  $\overline{\Sigma_{\text{tr}}}$  is the macroscopic transport cross section  $\Sigma_{\text{tr}}$  averaged over the depth-dependent energy spectrum (i.e.  $\varphi_{\text{FP}}$ )<sup>4</sup>, namely

$$\overline{\Sigma_{\text{tr}}}(z) = \int dE \varphi_{\text{FP}}(z, E) \Sigma_{\text{tr}}(z, E) / \int dE \varphi_{\text{FP}}(z, E),$$

with the macroscopic transport cross  $\Sigma_{\text{tr}}$  computed using the macroscopic elastic scatter cross section  $\Sigma_s$  via

$$\Sigma_{\text{tr}}(z, E) = \int_{-1}^1 d\mu \Sigma_s(z, E, \mu) (1 - \mu), \text{ with } \mu = \cos(\hat{\boldsymbol{\Omega}} \cdot \hat{\boldsymbol{\Omega}}').$$

There are multiple elastic scatter models that can be used to compute  $\Sigma_s$ . In this work, the two models that were investigated were the small-angle first Born approximation scatter model and Moliere's model (Scott 1963). Moliere's model provides improvements over the first Born approximation as it is valid for large angles, does not assume that the nucleus has infinite mass and includes the contribution of electronic screening of the nucleus. A comparison between these two models is shown in figure 1 where it can be seen that Moliere's model predicts an increased macroscopic elastic scatter cross section for all energies. This implies a larger transport cross section  $\Sigma_{\text{tr}}$  which in turn implies a larger variance of the lateral position of the FE solution that better matches the lateral profiles obtained from TOPAS.

## 2.2. Metric definition

The 6-dimensional phase-space density resulting from the individual solutions to the FP and FE equations can be used to obtain all clinically relevant metrics. For example, to compute the dose it is useful to introduce  $\Psi_{\text{FE}}$  as the angular integral of  $\varphi_{\text{FE}}$ , namely

$$\Psi_{\text{FE}}(\mathbf{r}) = \int_{4\pi} d\hat{\boldsymbol{\Omega}} \varphi_{\text{FE}}(\hat{\boldsymbol{\Omega}}, \mathbf{r}) = \frac{A^2}{2\pi \overline{\xi^2}(z)} \exp\left(-\frac{x^2 + y^2}{2\overline{\xi^2}(z)}\right), \quad (8)$$

and  $\Psi_{\text{FP}}$  as the energy integral of the  $S$ ,  $T$  and  $\Sigma_a$  terms from the FP equation (2), namely

$$\Psi_{\text{FP}}(z) = \int_0^\infty dEE \left[ -\frac{\partial S(z, E) \varphi_{\text{FP}}}{\partial E} - \frac{1}{2} \frac{\partial^2 T(z, E) \varphi_{\text{FP}}}{\partial E^2} + \Sigma_a(z, E) \varphi_{\text{FP}} \right]. \quad (9)$$

Then, if the CT image volume is given by the union of all of its  $N_v$  voxels (i.e.  $\mathcal{V} = \bigcup V_k, k = 1, \dots, N_v$  where  $V_k$  is the volume of one voxel), the energy  $E_k$  deposited by the proton beam in a voxel  $V_k$  is given by

$$E_k = \int_{V_k} dV \Psi_{\text{FE}}(\mathbf{r}) \Psi_{\text{FP}}(z).$$

The dose  $D_k$  in the same voxel  $k$  is given as

$$D_k = \frac{E_k}{m_k} = \frac{1}{\Delta V} \int_{V_k} dV \frac{\Psi_{\text{FE}}(\mathbf{r}) \Psi_{\text{FP}}(z)}{\rho_k},$$

<sup>4</sup> In the original formalism,  $\Sigma_{\text{tr}}$  depends on the average depth-dependent beam energy  $E_a(z)$ . It was found that weighing  $\Sigma_{\text{tr}}$  with the depth-dependent energy spectrum yields more accurate lateral profiles that better match MC results.

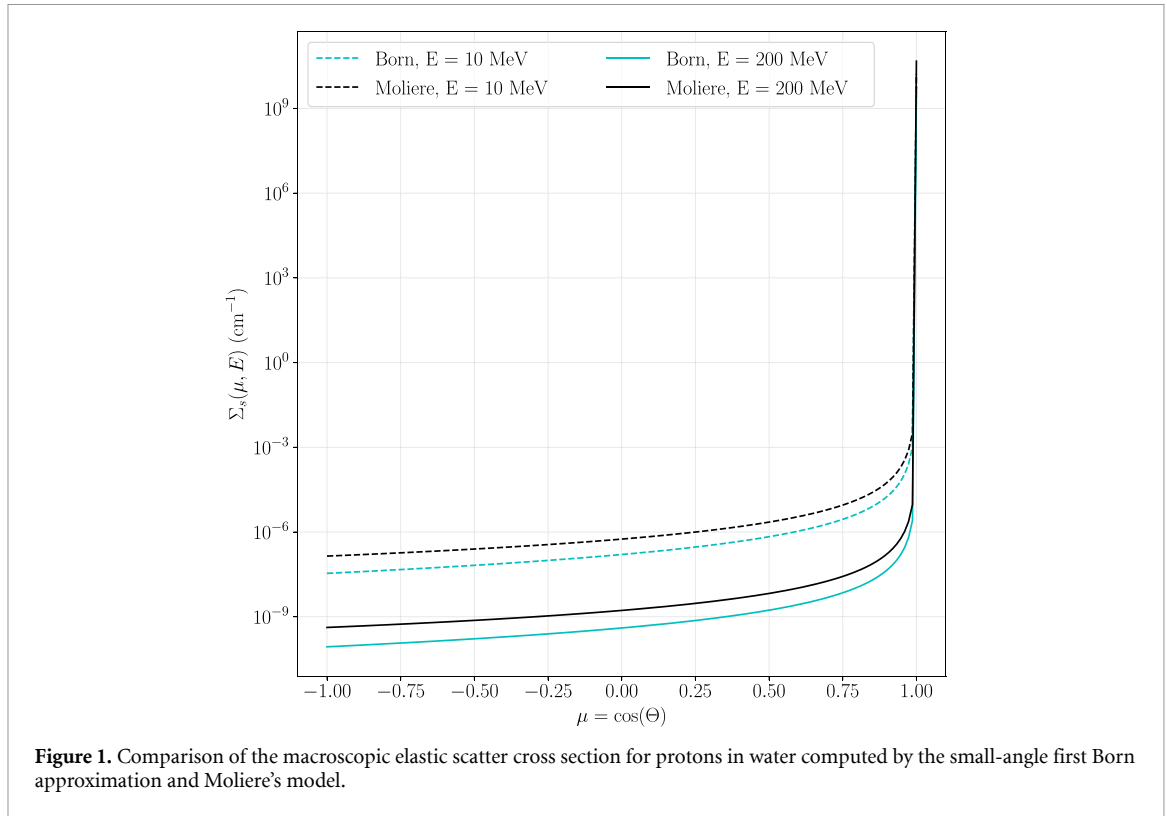


**Figure 1.** Comparison of the macroscopic elastic scatter cross section for protons in water computed by the small-angle first Born approximation and Moliere's model.

where  $\Delta V = \Delta x \Delta y \Delta z$  is the volume of a voxel  $k$  (constant for all voxels in the CT image) and  $\rho_k$  is the mass density of voxel  $k$ . Thus, the total dose in a certain region of interest (ROI) of the CT image, identified by the union of its corresponding voxels, is the sum of  $D_k$  over all  $k$  in the ROI.

### 2.3. Accounting for lateral heterogeneities

As equations (2) and (3) show, the formalism presented is inherently unable to account for heterogeneities located laterally to the central beam axis. To account for such cases, two modifications are introduced. First, the deposited energy density is multiplied by a laterally-dependent density scaling. This is physically motivated as the deposited energy is directly proportional to the local density. Second, each treatment plan spot (i.e. pencil beam) is decomposed into several sub-spots (i.e. beamlets) that are placed on concentric rings around the original spot position. The properties of the rings and of the beamlets on the rings are optimized for best performance.

#### 2.3.1. Lateral density scaling

The energy density in a voxel  $k$  is scaled by the ratio of the density  $\rho_k$  on the central beam axis at a depth that corresponds to the voxel  $k$  and the density  $\rho_k$  of the voxel itself, namely

$$E_k = \int_{V_k} dV \frac{\rho_k}{\rho_{ck}} \Psi_{FE}(\mathbf{r}) D_{FP}(z), \quad (10)$$

Using this scaling, the dose in voxel  $k$  becomes

$$D_k = \frac{1}{\Delta V} \int_{V_k} dV \frac{\Psi_{FE}(\mathbf{r}) D_{FP}(z)}{\rho_{ck}}. \quad (11)$$

Thus, a pencil beam distributes laterally a dose proportional to the density along the central beam axis.

#### 2.3.2. Optimized Gaussian beam splitting

On the boundary of the computational domain, the lateral dependence of the six-dimensional phase-space density is described by

$$\Psi_{FE}^{z=0}(x, y) = \int_{4\pi} \varphi_{FE}(x, y, z=0, \Omega_x, \Omega_y) d\hat{\Omega} = \frac{1}{2\pi\sigma_s^2} \exp\left(-\frac{(x^2 + y^2)}{2\sigma_s^2}\right), \quad (12)$$

where  $\sigma_s$  is the spatial standard deviation or spread of the  $x$  and  $y$  symmetric Gaussian. For the purpose of lateral beam splitting the original spot's central axis is placed at the origin of a 2D lateral grid. Given the radial symmetry of the Gaussian, placing sub-spots or beamlets on  $N_r + 1$  concentric rings with radii  $r_i$  around the original spot location was chosen, in a similar manner to Yang's method (Yang *et al* 2020). On a given ring  $i$  the beamlets share the same weight  $w_i$  and spread  $\sigma_i$ . The zeroth ring has a radius equal to zero and a single beamlet that is placed at the origin of the 2D lateral grid. Thus, the approximated fluence  $\Psi_{\text{FE}}^a$  is written as

$$\Psi_{\text{FE}}^a(x, y) = \sum_{i=0}^{N_r} \sum_{k=1}^{n_i} \frac{w_i}{2\pi\sigma_i^2} \exp\left(-\frac{(x-x_{ik})^2 + (y-y_{ik})^2}{2\sigma_i^2}\right),$$

$$x_{ik} = r_i \cos\left(\frac{2\pi k}{n_i} + \alpha_i\right), y_{ik} = r_i \sin\left(\frac{2\pi k}{n_i} + \alpha_i\right), \quad (13)$$

with  $n_i$  being the number of sub-spots placed on ring  $i$ ,  $(x_{ik}, y_{ik})$  are the coordinates of a sub-spot with index  $k$  on ring  $i$  and  $\alpha_i$  is a ring-dependent angular offset (meant to improve coverage for consecutive rings with the same number of beamlets). Prior to the optimization the number of rings  $N_r$ , the number of points on each ring  $n_i$  and the ring offsets  $\alpha_i$  are specified. As opposed to Yang's (2020) approach this formalism and implementation is not restricted to a number of pre-defined schemes. In principle any number of beamlets per ring and number of rings can be optimized. The optimization parameters (weights, spreads and ring radii) are collected in a vector denoted by  $\theta \in \mathbb{R}^{3(N_r+1)}$  with a structure of  $\theta = (\dots, w_i, r_i, \sigma_i, \dots)$ . The objective function of the optimization problem is defined as

$$J(\theta) = \iint_{-10\sigma_s}^{10\sigma_s} dx dy (\Psi_{\text{FE}}^a - \Psi_{\text{FE}}^{z=0})^2 / \iint_{-10\sigma_s}^{10\sigma_s} dx dy (\Psi_{\text{FE}}^{z=0})^2,$$

and is input into a scipy implementation of a trust-region constrained algorithm (Lalee *et al* 1998, Virtanen *et al* 2020). The weights  $w_i$  are bound constrained to be in the unit interval, namely  $0 \leq w_i \leq 1, \forall i = 0, \dots, N_r$  and are constrained such that

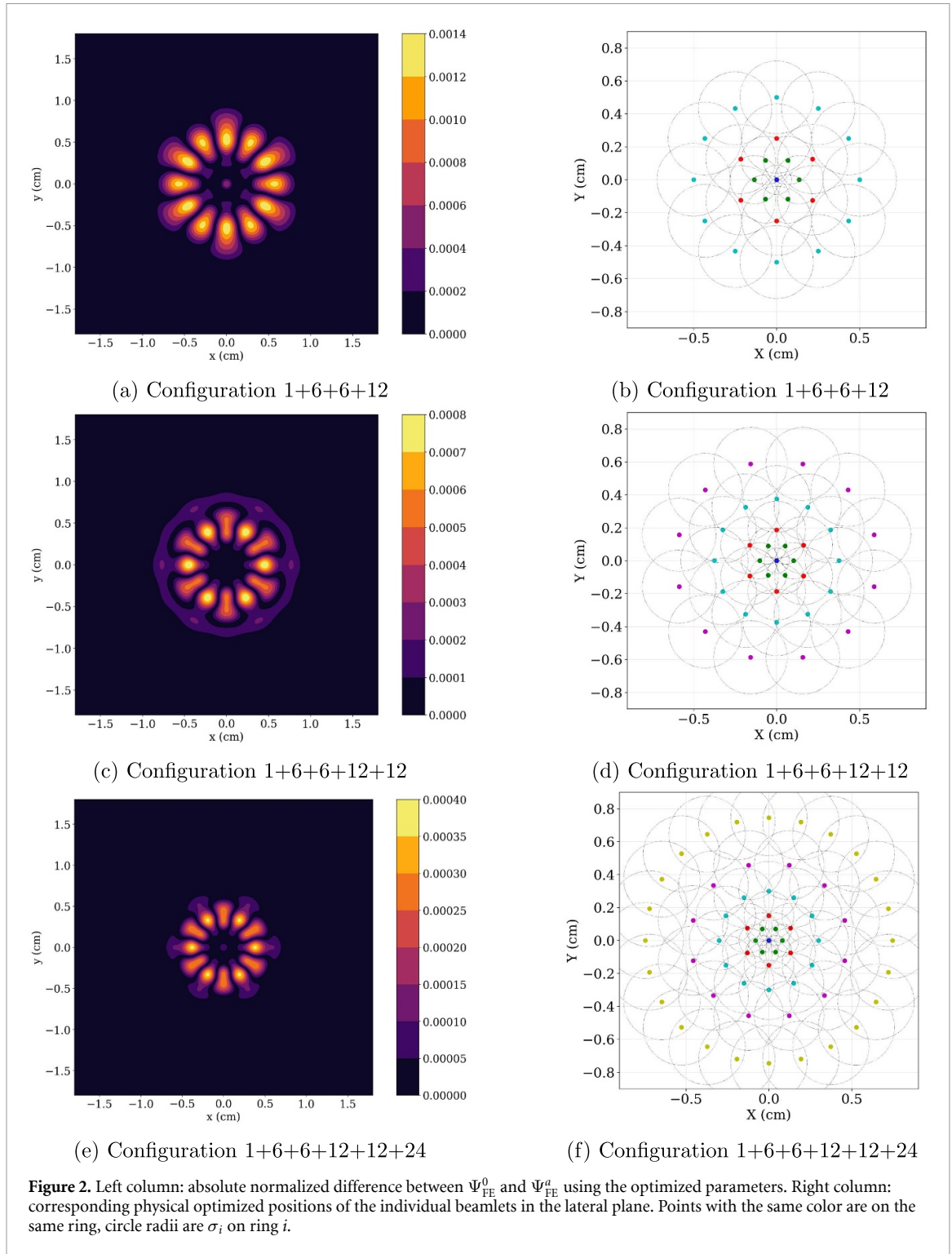
$$\sum_{i=0}^{N_r} w_i n_i = 1,$$

in order to ensure particle number conservation. To further guide the highly degenerate solution space towards useful splitting schemes, the ring radii are bound according to the initial spatial spread of the 2D Gaussian  $\sigma_s$  such that  $0 \leq r_i \leq r_{i+1} \leq 2\sigma_s$ . This evenly distributes the rings in  $[0, 2\sigma_s]$  and avoids optimal but less useful configurations where all the rings are placed close to one another and the origin. Similarly, the spreads of the rings  $\sigma_i$  are bound such that  $0.3\sigma_s \leq \sigma_i \leq \sigma_{i+1} \leq 0.8\sigma_s$ . The first ring should have the smallest spread so that errors coming from the central axis are limited. In the case of a spot with an initial spread of  $\sigma_s = 0.3$  cm figure 2 shows for three different splitting schemes the absolute difference between  $\Psi_{\text{FE}}^{z=0}(x, y)$  and  $\Psi_{\text{FE}}^a(x, y)$  in the left column and the actual positions of the beamlets on the concentric rings together with the optimized spreads (indicated by the circle radii) around each spot in the right column.

## 2.4. Metric change computation

Next to its dose computation capabilities, an advantage of YODA is the ease of applying the adjoint method. This general mathematical framework approximates to first order the change in a metric as a function of the change in all independent variables. Examples of possible independent variables are HU values in the CT image or treatment plan spot characteristics such as mean energy, energy spread, position, MU value (or equivalently the number of protons), angular spread and the spot size. Examples of metrics are the mean dose to an OAR or NTCP values. The adjoint method is useful when the number of independent variables is large (so that re-computing the metric for each new variable becomes prohibitively expensive) and their change is relatively small (so that the first order adjoint approximation is accurate). Since CTs typically have millions of voxels, this is likely always the case in radiotherapy. Examples of applications are computing dose or NTCP differences caused by differences between planned and delivered spot MU values or isocenter positions or by delivering yesterday's treatment plan on today's CT image. This section provides only the main details of the adjoint method for the case when the independent variables that change are the HU values of the CT image and the metric considered is the dose in a voxel  $V_k$ . Larger regions of clinical interest are trivial generalizations of this case.

A given change in the HU values of the CT image implies two distinct changes in the deposited dose  $D_k$  in the voxel  $k$ . One is a direct change, since a HU change in the voxel  $k$  implies, among others, a stopping power



change which can be directly inputted in the  $D_k$  change via equation (9). The other is an indirect change, as a stopping power change somewhere along the proton beam path implies a proton flux change in the considered voxel  $k$ . This change can only be known by re-solving for  $\varphi$  from the FP equation (2) and the FE equation (3) with the new HU values. Thus, the change in  $D_k$  is written as,

$$\delta D_k = \delta D_{k,\text{dir}} + \delta D_{k,\text{indir}},$$

where  $\delta$  denotes a variation,  $\delta D_{k,\text{dir}}$  denotes the part of  $\delta D_k$  that can be directly computed and  $\delta D_{k,\text{indir}}$  denotes the part that would have to be re-computed.

The adjoint method removes from  $\delta D_k$  the part  $\delta D_{k,\text{indir}}$  that would have to be re-computed and in this process computes a first order approximation to  $\delta D_k$ . This is done by expressing  $\delta D_{k,\text{indir}}$  as an inner product

between two quantities. One is the change in the proton flux  $h_\varphi$  caused by the change in the HU values and the other is a vector denoted by  $r^\dagger$ , namely  $\delta D_{k,\text{indir}} = \langle h_\varphi, r^\dagger \rangle$ . The vector  $r^\dagger$  is identified as the right-hand side of a new system called the adjoint system. This system is written as  $L^\dagger \varphi^\dagger = r^\dagger$  and its solution is called the adjoint flux  $\varphi^\dagger$ . Using this together with the properties of the adjoint system  $\delta D_{k,\text{indir}}$  is expressed as

$$\begin{aligned} \delta D_{k,\text{indir}} &= \langle h_\varphi, r^\dagger \rangle = \langle h_\varphi, L^\dagger \varphi^\dagger \rangle = \langle L h_\varphi, \varphi^\dagger \rangle = -\langle \delta L \varphi_{\text{FP}}, \varphi^\dagger \rangle \\ &= \iint dE dz \varphi^\dagger(z, E) \left[ -\frac{\partial \varphi_{\text{FP}}}{\partial z} + \frac{\partial \delta S \varphi_{\text{FP}}}{\partial E} + \frac{\partial^2 \delta T \varphi_{\text{FP}}}{\partial E^2} - \delta E_a \varphi_{\text{FP}} \right], \end{aligned} \quad (14)$$

where  $\delta S, \delta T, \delta \Sigma_a$  are the changes in the stopping power, straggling coefficient and macroscopic absorption cross section caused by the change in the voxel HU value. Thus, if there are  $N_{HU}$  values for which the dose in the voxel  $k$  is desired, re-computing would cost  $N_{HU}$  FE and FP solutions. In contrast, the adjoint method only performs two FE and FP solutions and  $N_{HU}$  inner products. The construction of the right hand side  $r^\dagger$  and of the adjoint operator  $L^\dagger$  is illustrated in our previous work (Burlacu *et al* 2023). This approach can be advantageous for the time constrained cases when the changes in the CT image HU values are small enough. For such cases, the adjoint method can provide significant time savings by avoiding an expensive re-computation of the treatment plan on the new CT image.

### 3. Results and discussion

#### 3.1. Dose engine performance

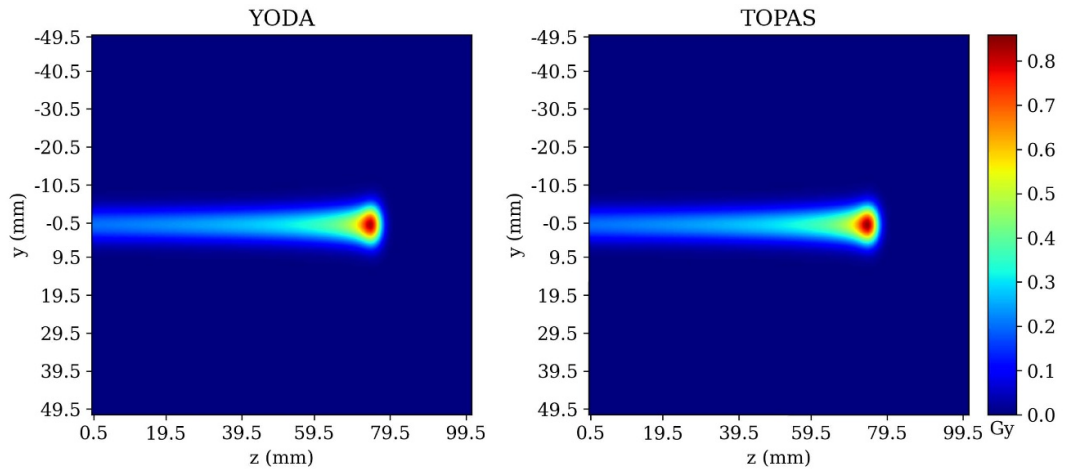
The dose engine of YODA was benchmarked against TOPAS in several irradiation test-cases such as homogeneous and heterogeneous water tanks, head and neck (H&N), prostate and lung CTs. TOPAS simulations were performed using the em-opt4 physics list which is the most accurate modelling of electromagnetic interactions available within TOPAS. Nuclear interactions were excluded from this comparison as YODA does not currently account for nuclear interactions. In all TOPAS simulations the number of protons per spot was set to  $1.0 \times 10^8$  and the maximum number of available cores (48) was used. Using this physics list and number of cores, the run-times of TOPAS were in the order of hours. In all test cases, a YODA spot was split according to a 1 + 6 + 6 + 12 + 12 + 24 Gaussian beam splitting scheme as this was found to yield accurate results when compared to TOPAS. For this splitting scheme on average one spot takes 2 s to compute. Additional speed-ups could be achieved in two ways. One is to address the main speed limitation (memory access bandwidth) by implementing the algorithm on a graphics processing unit (GPU) card. The second is to implement an adaptive energy grid on a per sub-spot level. Currently the energy grid is divided into a fixed number of groups which results in the majority of the groups and thereby the system solved at each step being empty. By adapting the energy grid to be finely discretized in the locations in energy where the flux has significant values and coarse everywhere else significant speed-ups can be expected.

##### 3.1.1. Simplified tank geometries

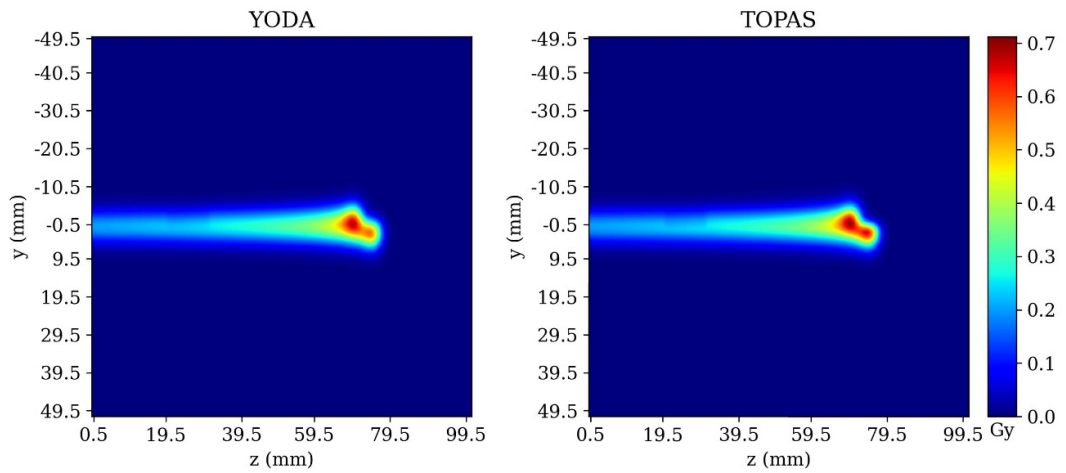
First, three tank-based tests, that are typical for benchmarking pencil beam algorithms, were performed. In all three cases, a tank (of dimensions of  $10 \times 10 \times 10 \text{ cm}^3$ ) was irradiated with a spot with nominal energy 100 MeV, an energy spread of 1 MeV, a spot size of 0.3 cm, an angular spread of  $1.0 \times 10^{-8}$  rad and a correlation of 0. The first case, denoted by (a), is the one in which the tank is composed homogeneously of water (0 HU). In the other two cases, a half-plane slab is introduced in the tank between 2 and 3 cm in depth in the upper-half of the  $x$ - $y$  plane (with  $z$  being the depth). This is usually one of the most challenging geometries for pencil beam algorithms. In one case, denoted by (b), the slab was composed of bone-like tissue of 1000 HU and in the other, denoted by (c), it was composed of air-like tissue of  $-1000$  HU. The tank was created using an in-house DICOM CT scan writer and was composed of  $100 \times 100 \times 100$  voxels with a voxel size of  $0.1 \times 0.1 \times 0.1 \text{ cm}^3$ . Two-dimensional slices of the dose distributions of YODA and TOPAS can be seen in figure 3. Integrated depth doses (IDDs) and lateral profiles at different depths along the original spot axis can be seen in figure 4.

For these simple test cases, the visual agreement is excellent, as illustrated by both figures 3 and 4. This is also reflected in the 3D gamma index pass rates shown in table 1 under the columns denoted by  $-1000$  HU, 0 HU and 1000 HU. The worst passing rate using the strict 1 mm, 1%, 10% dose cutoff is 98.22%. All passing rates presented can be further improved by fine tuning the splitting scheme. One way of doing so is to increase the number of rings. Another, is to take advantage of the underlying CT grid in the case of this perpendicular propagating spot. If in the lateral beam eye view grid, one beamlet is placed per voxel and the spread is contained to the voxel lateral dimensions, the error is bound to decrease without much increase in computational cost.

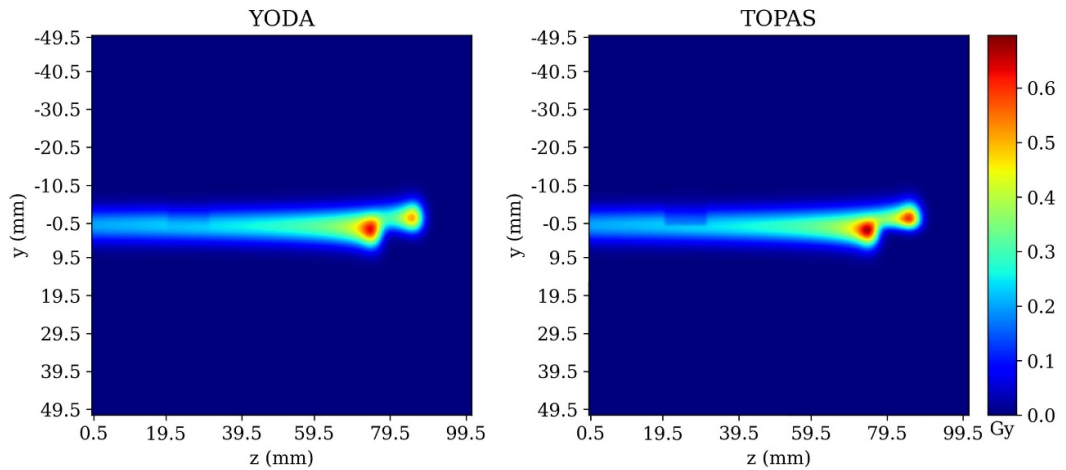
Next to the simple geometries, a more challenging sliding slab experiment was also performed. In this experiment, the slab is moved with respect to the central axis of the beam from  $-4$  mm to 4 mm in



(a) Comparison in a homogeneous 0 HU tank



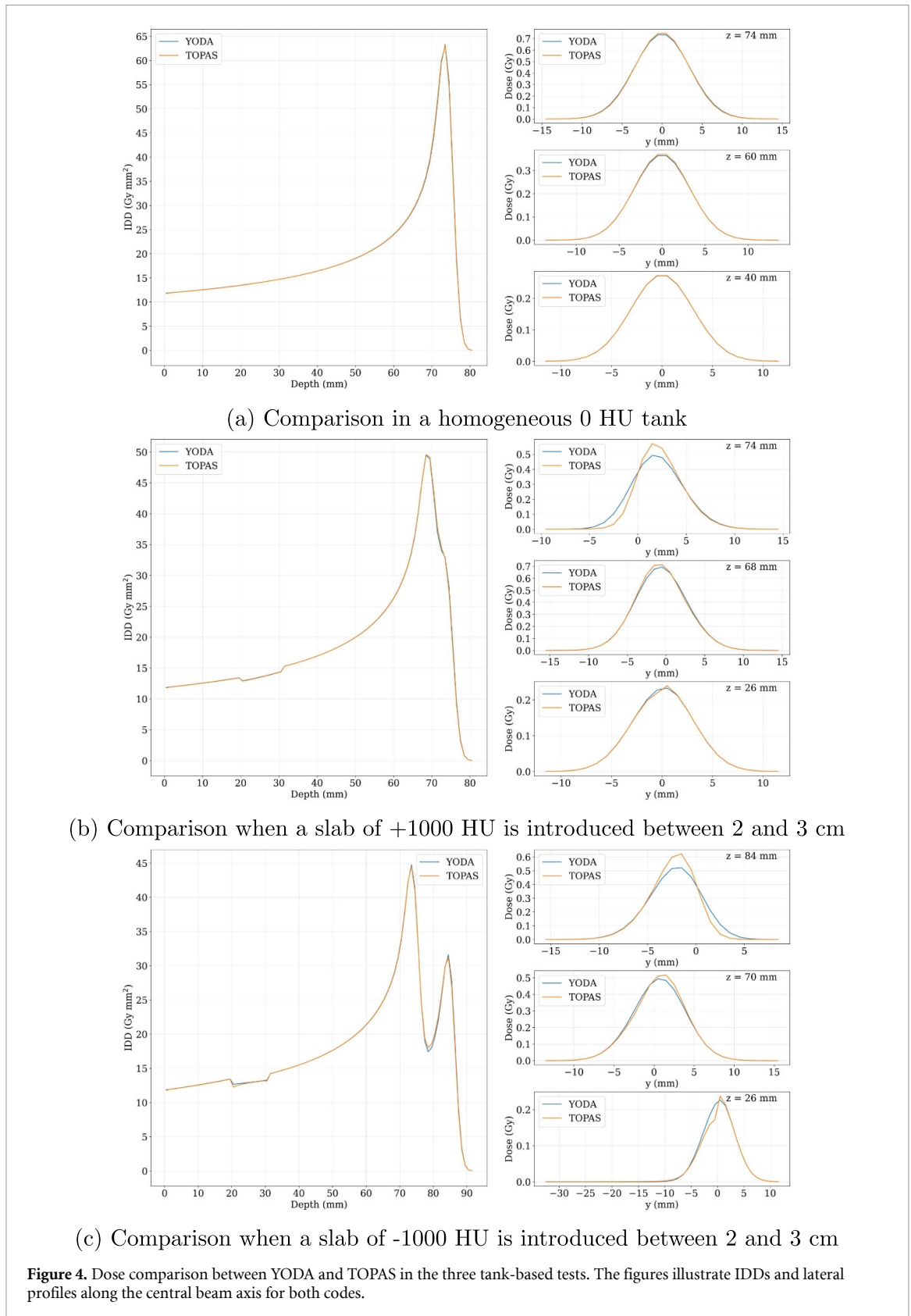
(b) Comparison when a slab of +1000 HU is introduced between 2 and 3 cm



(c) Comparison when a slab of -1000 HU is introduced between 2 and 3 cm

**Figure 3.** Dose comparison between YODA and TOPAS in the three tank-based tests. The figures illustrate 2D dose slices along the central beam axis for YODA in the left column and for TOPAS in the right column.

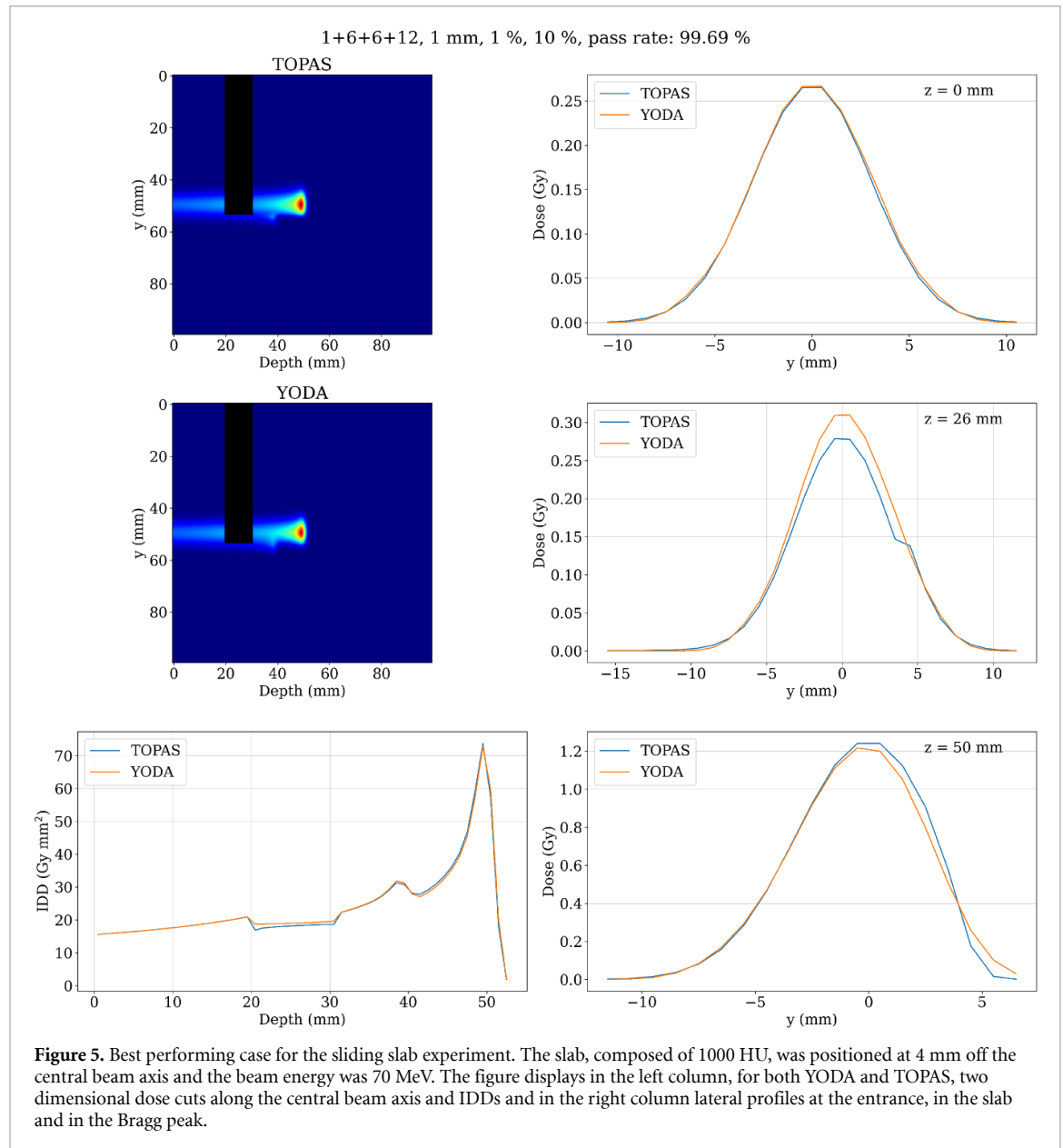
increments of 2 mm. As in the previous tests, the composition of the slab is set to either -1000 HU or 1000 HU and its depth is kept between 2 cm and 3 cm. To assess the accuracy of the dose algorithm across the clinical energy spectrum, beam energies of 70 MeV, 160 MeV, 190 MeV and 230 MeV are tested. The beam spread is set to 1.0 in TOPAS, which implies spreads of 0.7 MeV, 1.6 MeV, 1.9 MeV and 2.3 MeV. The remaining beam characteristics are kept identical to the previous test cases, i.e. a spread of 0.3 cm, an angular spread of  $1.0 \times 10^{-8}$  rad and a correlation of 0. Figures 5–7 show the best, average and the worst cases of



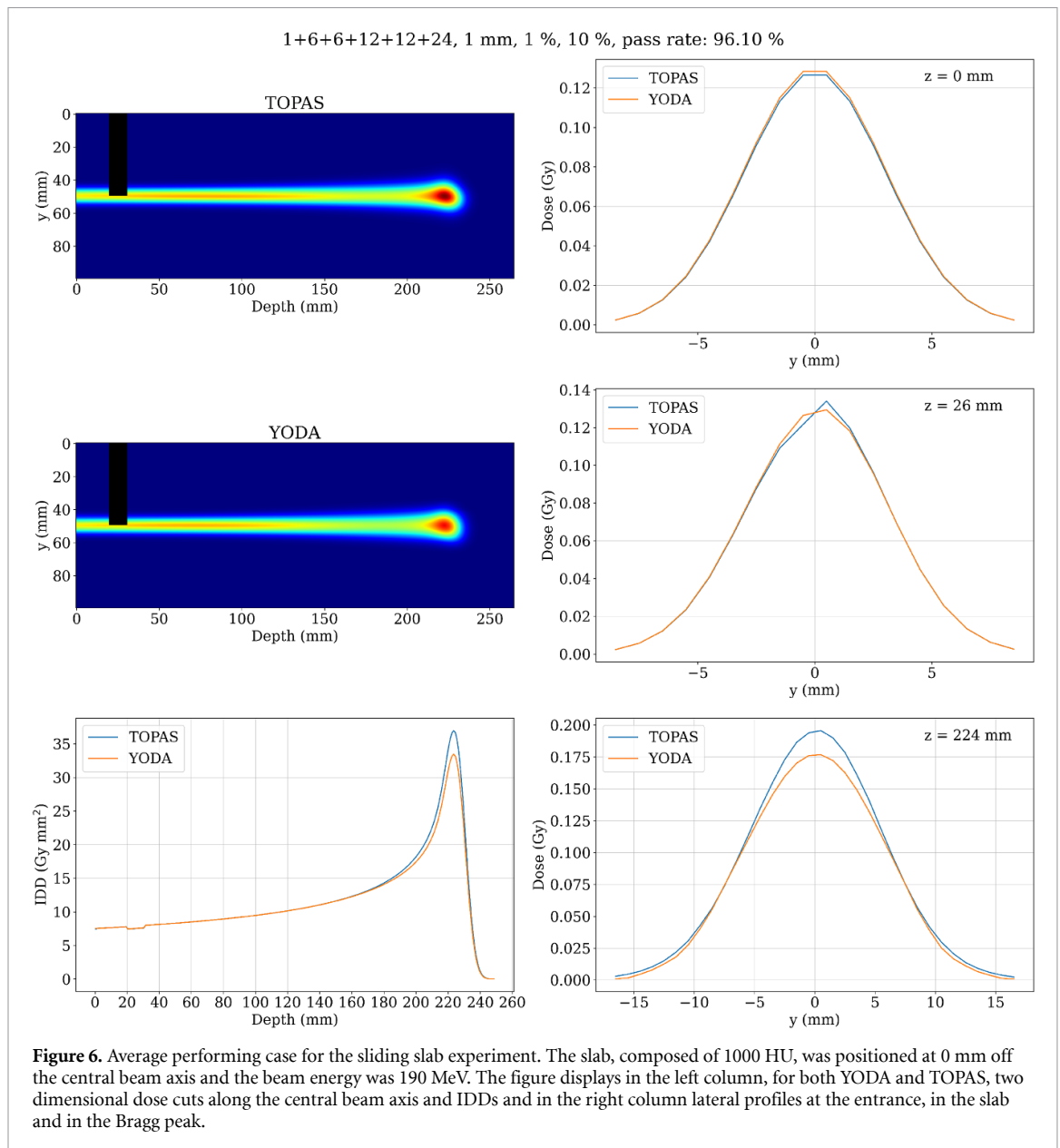
these tests. A full overview of the 120 test cases is presented in the tables 2–9 from appendix. Despite the broad range of energies and challenging lateral heterogeneities encountered, the experiment shows that YODA computes doses with high passing rates using the strictest gamma index criteria. In addition to the conclusions drawn from table 1, the tables presented in appendix provide three main findings. One, more beams do not necessarily imply a more accurate result. This is supported by table 9, where a simpler beam splitting scheme of 1+6+6+12 often performs better than the more complex 1+6+6+12+12+24 one. This

**Table 1.** Gamma index passing rates for different criteria and test cases.

Criteria			Gamma index						
			Passing rates (%) for						
mm	%	%—cutoff	−1000 HU	0 HU	+1000 HU	H&N	Prostate	Lung 1	Lung 2
1	1	0	99.96	100	99.99	100	100	100	99.99
1	1	10	98.22	99.93	99.45	99.85	99.58	95.62	94.55
2	2	0	100	100	100	100	100	100	100
2	2	10	99.61	99.95	99.78	99.99	99.99	99.72	98.09
3	3	0	100	100	100	100	100	100	100
3	3	10	99.73	100	99.85	99.99	100	99.86	99.12



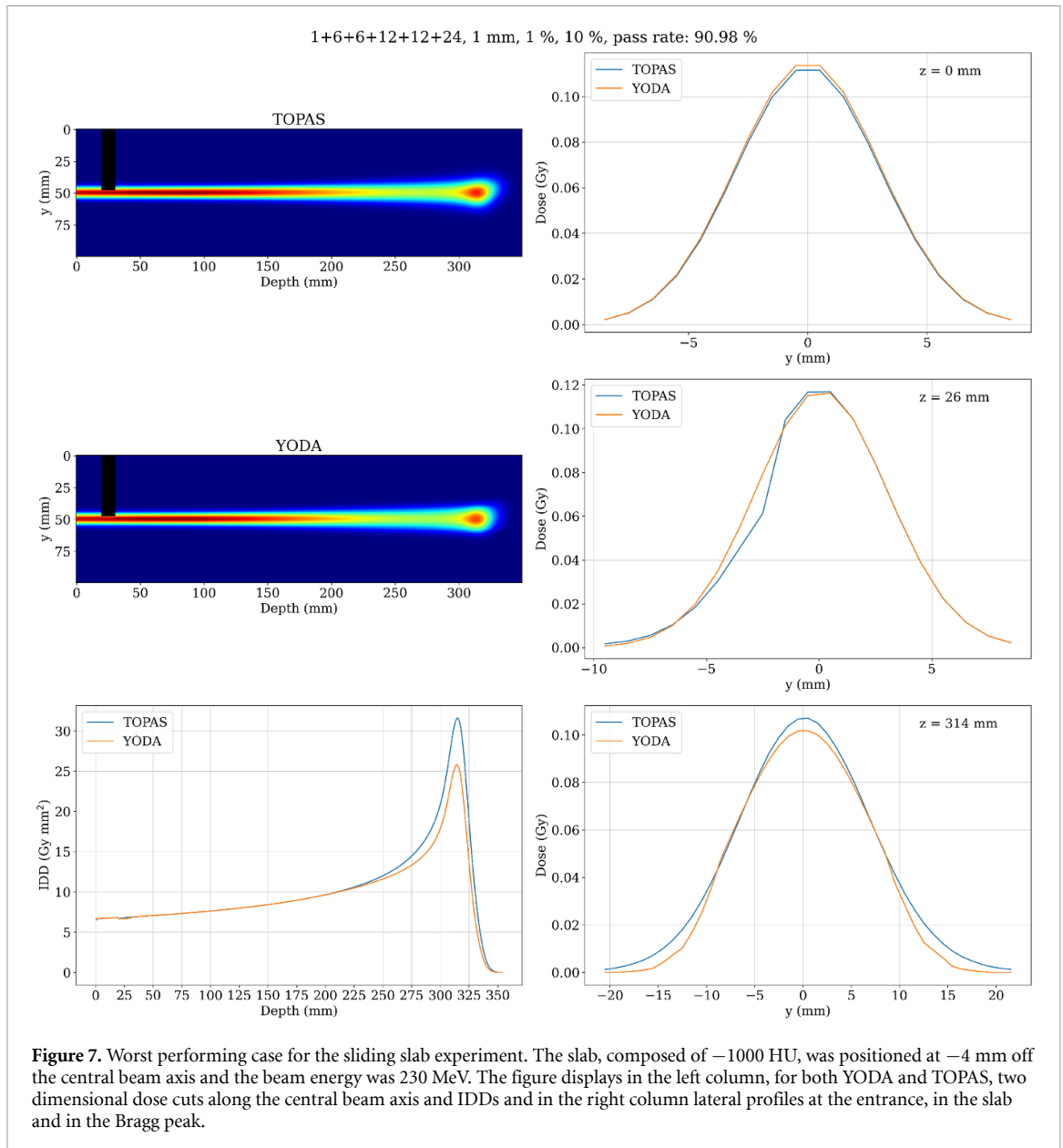
is likely due to the interplay of several factors. The chosen beam size, the underlying CT grid size (and the projection of this in the beam-eye view coordinate system), the specific location on the rings of the optimized sub-spots and the location of the heterogeneity itself all play a role in the accuracy of a given scheme. Given this, and the fact that in a realistic treatment plan spots are placed in close proximity one to another, it is likely that YODA will result in accurate and quickly computed doses using simpler beam splitting schemes. Second, as already illustrated in table 1 and further illustrated in tables 4 and 5 the accuracy of YODA with respect to TOPAS is slightly worse when air gaps are placed in the beam path. Such



small differences can arise due to the inherent limitations of the FE modelling and the different modelling of Coulomb elastic scattering in air between the two codes. Third, there is a slight degradation of accuracy occurring towards the high part of the energy spectrum (effect that was not observed towards the low part of the energy spectrum). This could be explained by a number of factors. The first one comes from differences in the underlying data that the two codes use. The stopping powers were extracted from TOPAS using increasingly coarse steps in energy towards the high side of the energy domain. This can cause slight range differences, especially as the stopping power is linearly interpolated in the energy groups, which in turn can result in range differences. Differences in stopping power imply differences in lateral scattering which contribute to further differences. Moreover, the straggling coefficient is computed using an analytical equation that could prove inaccurate for the high energy part of the domain. Despite these differences, the gamma index pass rate using the strictest criteria and a splitting scheme of 1+6+6+12 does not fall below  $\approx 95\%$  for energies above 190 MeV for all the tested geometries.

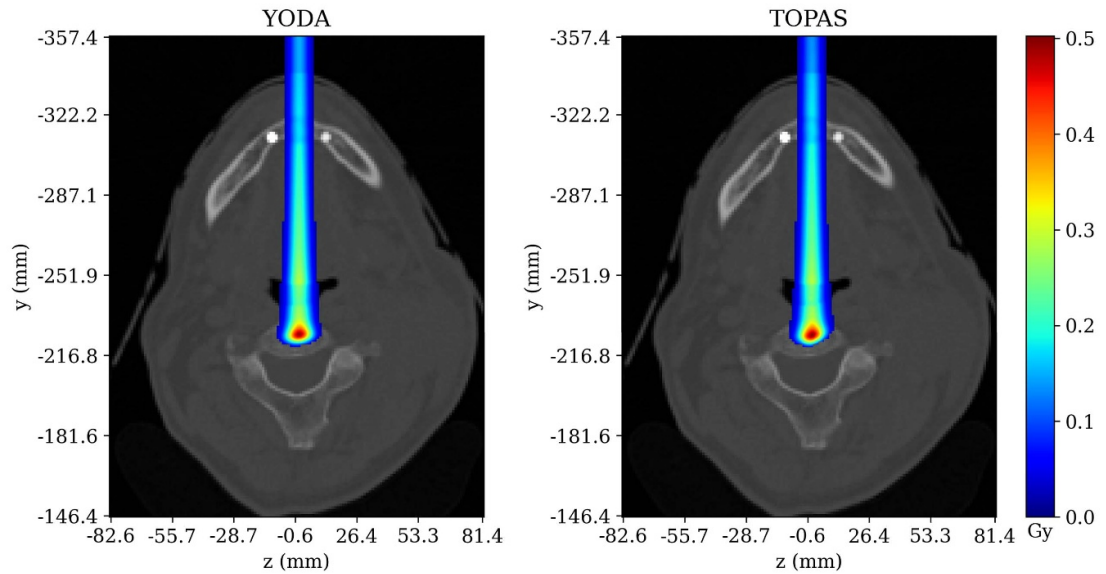
### 3.1.2. CT based anatomies

In addition to the tank-based tests, three real CT images were also tested. The H&N scan was taken from the CORT dataset (Craft *et al* 2014), the prostate scan was taken from the cancer imaging archive (Yorke *et al* 2019) and the lung scan was taken from the Holland Proton Therapy Center (Pastor Serrano 2023). The used isocenter locations and gantry angles are not meant to be clinical and were chosen only due to their simplicity of set-up in TOPAS.

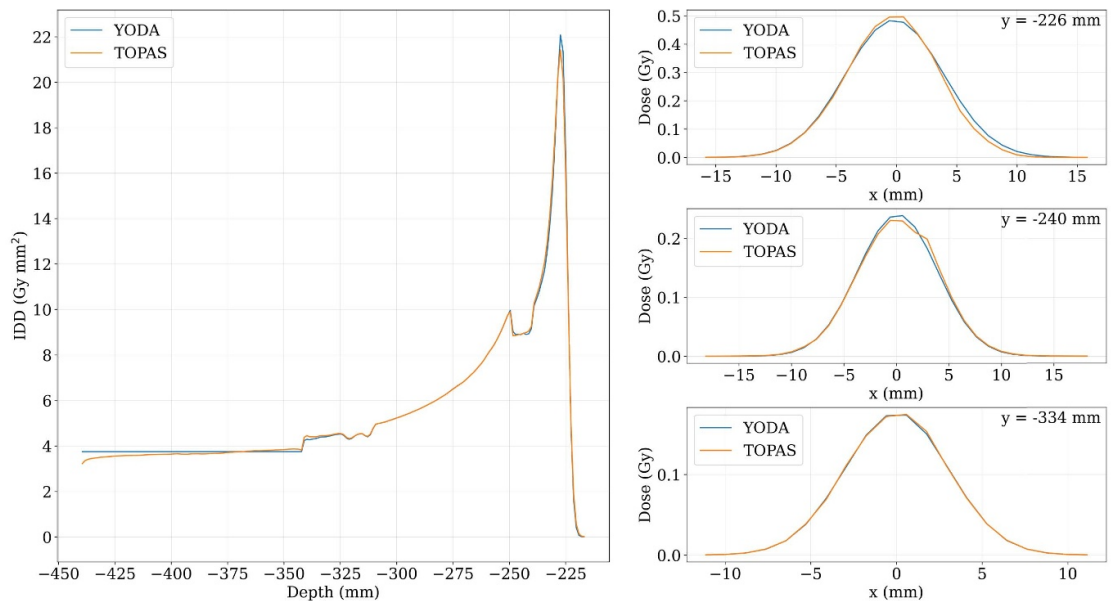


In the H&N case, one spot was irradiated with the beam impinging along the  $y$  axis (i.e. at a gantry angle of  $0^\circ$ ) with a nominal beam energy of  $125$  MeV with the isocenter being the center of the CT scan volume. The two dimensional dose profile can be seen on the top row of figure 8 and the IDD and lateral profiles at three depths can be seen at the bottom of figure 8. Good agreement is observed, as the 99.85% gamma index pass rate from the H&N column of table 1 also shows. Figure 8 shows a discrepancy in the air region between  $-440$  mm and  $-340$  mm. This is also the case for the lung and prostate cases visible figures 9 and 11. Two possible reasons are differences in the modelling of air between the two algorithms or a slight mismatch in the positioning of the beams with respect to the CT grid caused by the placement of the beam at the interface of voxels. Given that the agreement is good in the clinically relevant region of the scan this discrepancy is deemed acceptable.

The lung scan was irradiated with two spots where one beam goes from  $-x$  to  $+x$  and the other in the opposite direction (i.e. at  $90^\circ$  and  $270^\circ$  gantry angles respectively). Both spots had a mean energy of  $125$  MeV, energy spread of  $1$  MeV, a spot size of  $0.3$  cm, an angular spread of  $1.0 \times 10^{-8}$  rad and a correlation of  $0$ . This case is denoted by Lung 1. Given the challenging anatomy, the results from figure 9 together with the passing rate of 95.62% from the Lung 1 column of table 1 are very good. To further test YODA's dose engine performance, a second test for the lung was performed where the BP was moved towards a more heterogeneous area by changing the beam energies. In this case, one beam had an energy of  $105$  MeV with a spread of  $0.84$  MeV and the other an energy of  $135$  MeV with a spread of  $1.08$  MeV. This case was denoted by Lung 2. Here too, despite the challenging heterogeneous anatomy, YODA performs well given that the worst



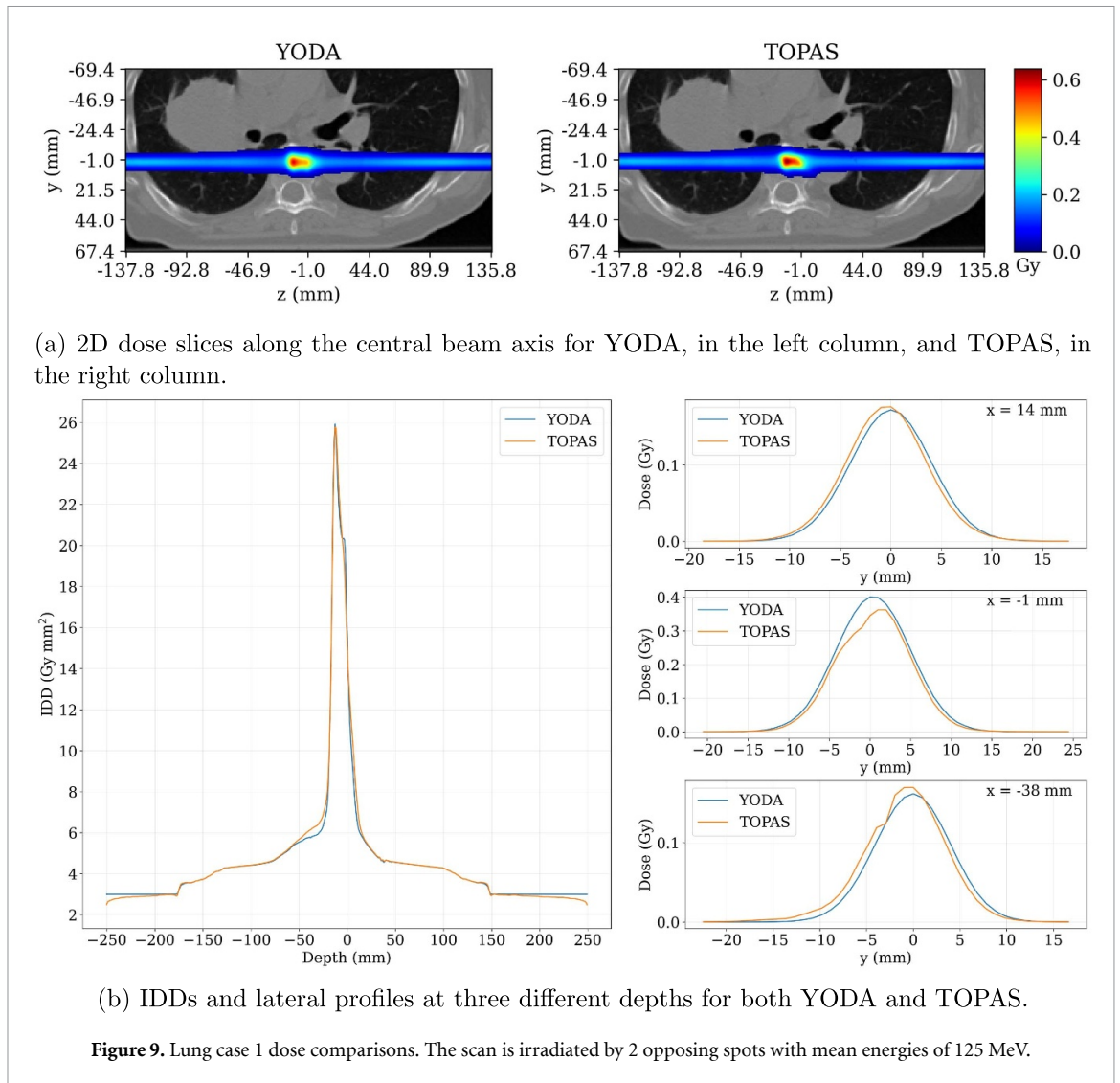
(a) 2D dose slices along the central beam axis for YODA, in the left column, and TOPAS, in the right column.



(b) IDD and lateral profiles at three different depths for both YODA and TOPAS.

**Figure 8.** H&N test case dose comparisons. The scan is irradiated by one spot of 125 MeV.

gamma index passing rate is 94.55% (as seen in column Lung 2 in table 1). Two dimensional profiles, IDD comparisons and lateral profiles can be seen in figure 10. The lateral profiles from figure 9 show a consistent lateral shift between YODA and TOPAS at the 14 mm,  $-1$  mm and  $-38$  mm depths. A reason for this could be the initial location of the Gaussian split sub-spots on the CT scan surface. The spots are generally not aligned with the CT grid (as such alignment is only possible in cases of perfectly perpendicular beams) and therefore slight asymmetries could arise if spots are placed exactly at the interface of voxels. The accuracy can be improved by fine-tuning the Gaussian beam splitting scheme in several ways. One is to include the number of rings and the number of beamlets per ring into the optimization procedure itself. Another is to consider alternative, non-concentric sub-spot arrangements. A metric for lateral heterogeneity could help in guiding the optimization towards sparsely placing beamlets in areas of low heterogeneity and more densely covering areas with high heterogeneity. Lastly, a progressive splitting scheme could also be employed, whereby once a threshold of lateral heterogeneity has been reached, the beamlets encountering it are re-consolidated and a new (finer) split occurs. Given that the parameters of such schemes can be pre-optimized and tabulated the computational increase of such an approach could be kept minimal.



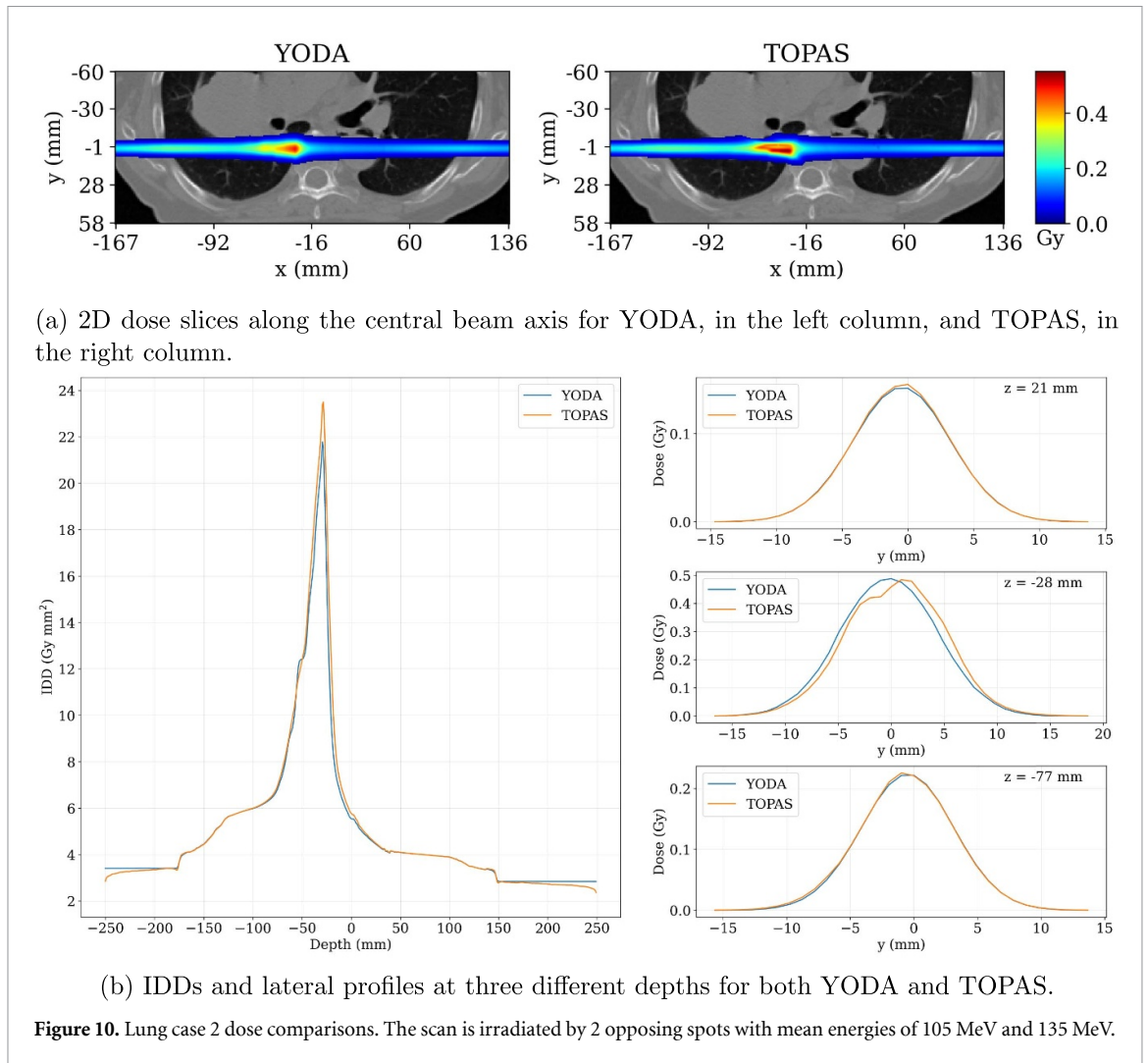
The prostate case set-up was identical to that of the lung with the only difference being the spot mean energy of 165 MeV and the spot energy spread of 0.825 MeV. Here again the agreement is very good as seen in figure 11 and by the high passing rate of 99.58% from the prostate column of table 1.

### 3.2. Dose change computations

In addition to the dose engine performance, the performance of the dose change computation was also benchmarked. Given a specific volume within the CT scan denoted as ROI, the adjoint component is able to cheaply and accurately compute the change in the dose deposited in the ROI (for small enough anatomical perturbations). The speed of such an operation far exceeds that of plain re-computation as effectively, the only computation necessary comes in the form of vector inner products. This could be employed in an online re-adaptation trigger system where YODA assesses the effect of delivering yesterday's plan on today's anatomy. The benchmark starts with the same simplified tank test-cases and thereafter moves toward more realistic cases using RT plans for clinical RT structures on CT images.

#### 3.2.1. Simplified tank geometries

In the case of the simple tank geometries, the adjoint component used a ROI defined as everything past the depth of 60 mm in the tank. The composition of the half-slab was varied from  $-1000$  HU to  $1000$  HU. The mean dose deposited in the ROI was computed for each new geometry using two methods: re-computations and adjoint computations. Figure 12 shows the mean dose deposited in the ROI as a function of the HU composition of the slab. The two lines are close one to another around the value of 0 HU which was considered the base case and they start to diverge towards the edges of the HU domain. The maximal relative

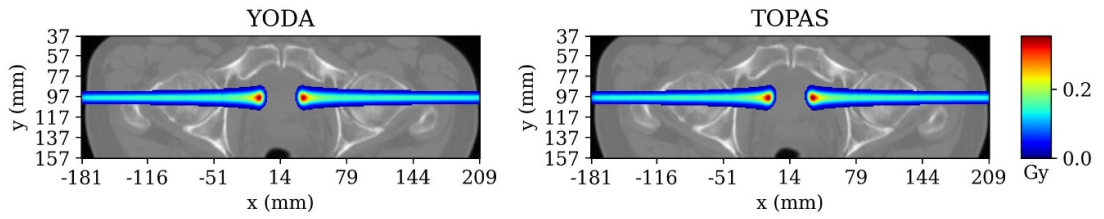


error of 2.2% occurs at the  $-1000$  HU end of the HU domain. Based on these results, it can be concluded that the adjoint component is capable of cheaply and accurately computing the change in the deposited dose in the ROI for this test case.

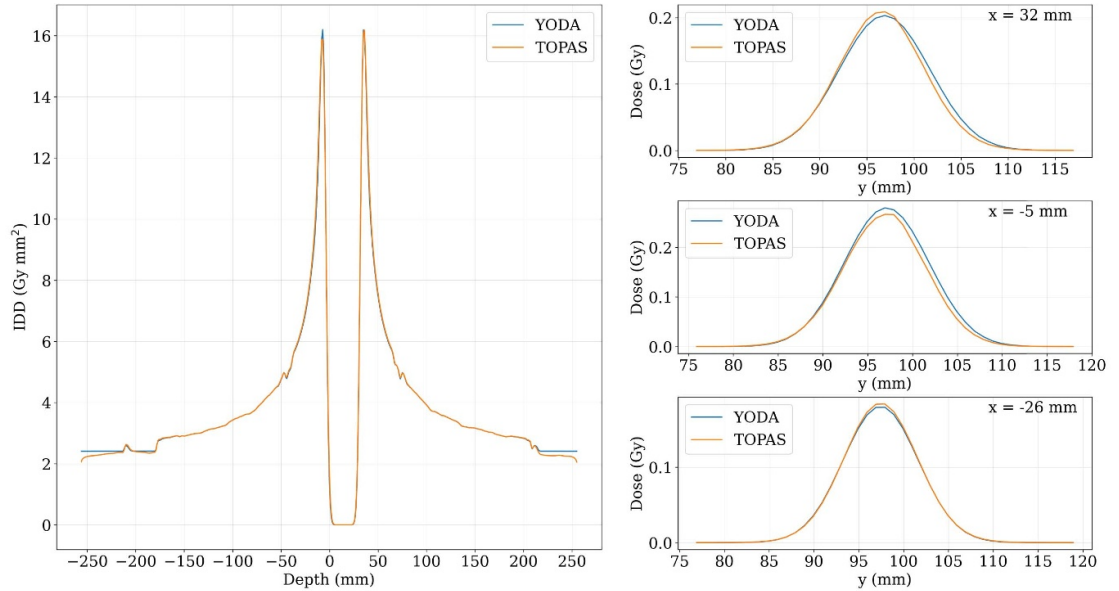
### 3.2.2. Treatment plan tests

Four treatment plans for the gross tumor volume (GTV) were generated for two H&N patients (patients 1 and 2) in Raystation (Bodensteiner 2018). For both patients, one robustly and one non-robustly optimized plans were created. The plans are not clinical and are only used for the purpose of creating conformal doses around the target. Patient 1 had plans that contained roughly 1000 spots and patient 2 had plans with roughly 300 spots. Both plans were split according to a  $1 + 6 + 6 + 12$  Gaussian beam splitting scheme. Each patient had multiple repeat CTs (rCTs) which were registered to the planning CT (pCT) using the simple-itk library (Beare *et al* 2018). The adjoint component computed the change in the GTV dose caused by the new CT image. This is meant to simulate the situation of a daily re-adaptation trigger system where the effect of yesterday's plan is assessed on today's anatomy. As long as the anatomical changes between the planning and repeat CT images are not too large, the adjoint component is accurate and fast as it does not require re-computing the original plan on the new image.

Figures 13 and 14 show each of the CT images for patient 1 (image number 0 is the planning image), a 2D dose slice of the re-computed dose distribution on the CT image, the GTV dose computed via re-computation and via the adjoint component and the relative error between these two results. In the case of a non-robustly optimized plan, the adjoint component attains a maximal error of 5.5% as presented in



(a) 2D dose slices along the central beam axis for YODA, in the left column, and TOPAS, in the right column.



(b) IDD and lateral profiles at three different depths for both YODA and TOPAS.

Figure 11. Prostate case dose comparisons. The scan is irradiated by 2 opposing spots with mean energies of 165 MeV.

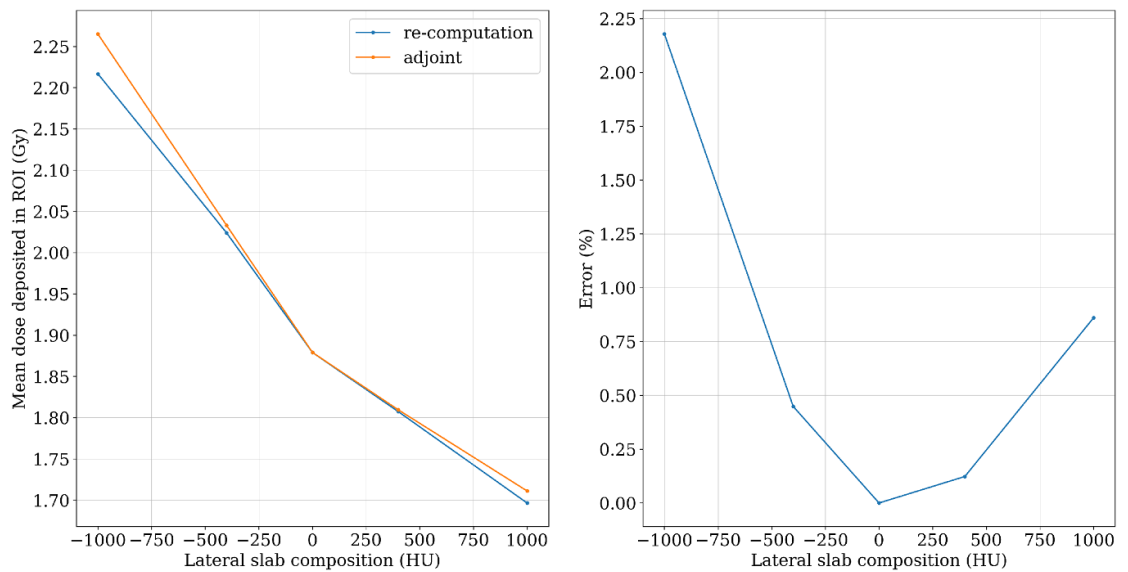


Figure 12. On the left the re-computed versus adjoint computed doses for the simplified tank geometries are displayed. On the right, the error, in percentages, between these two quantities is displayed.

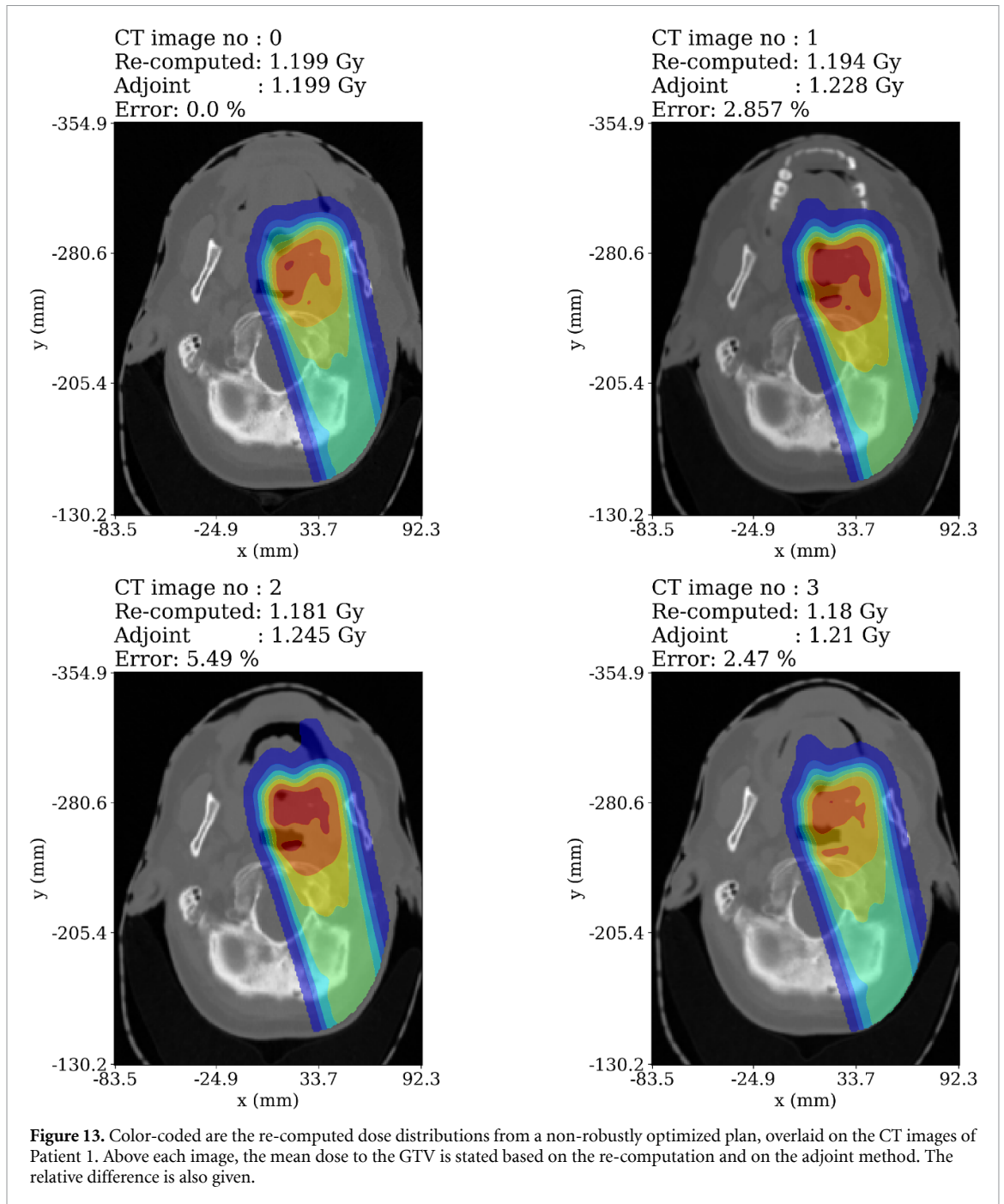
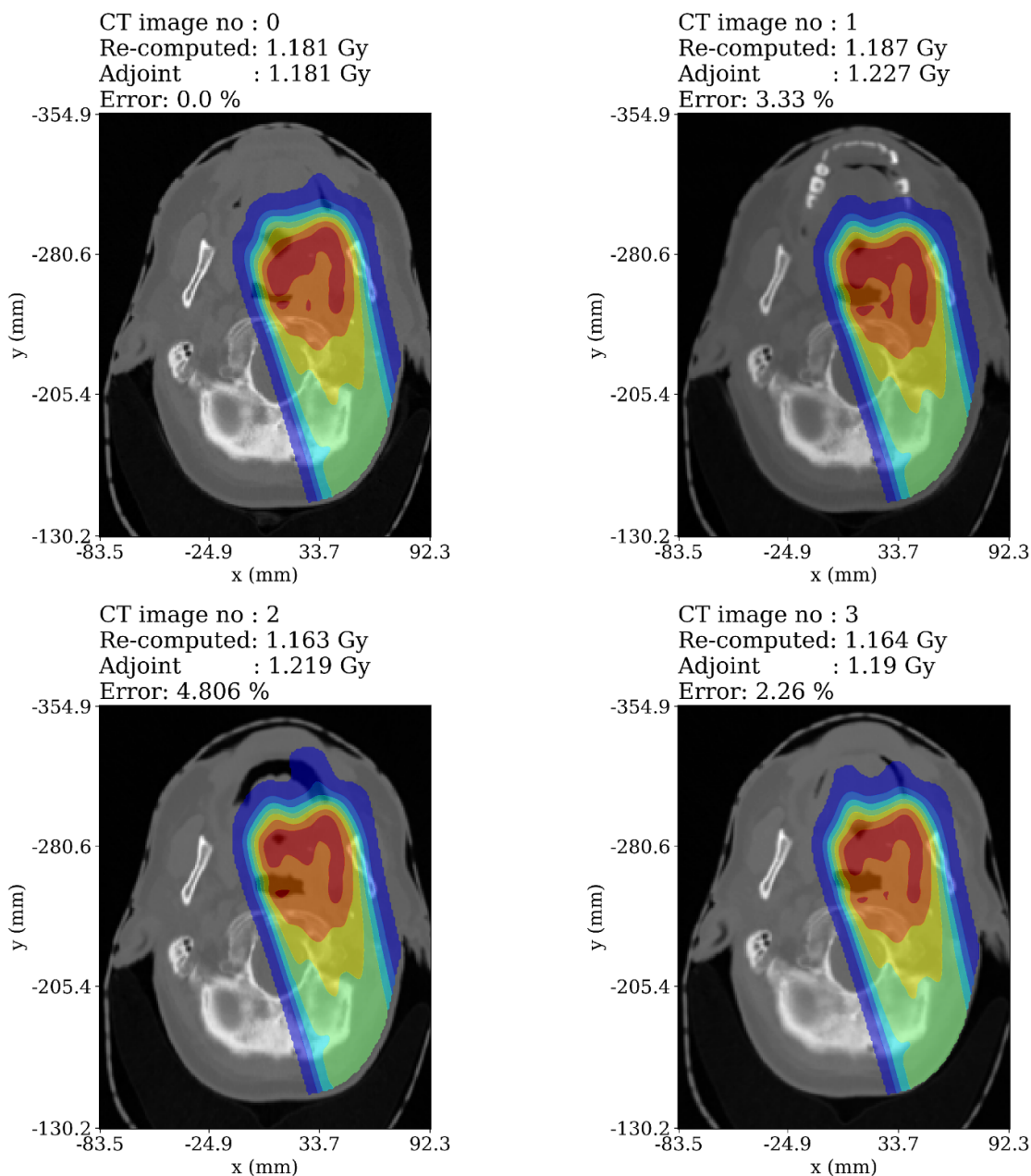
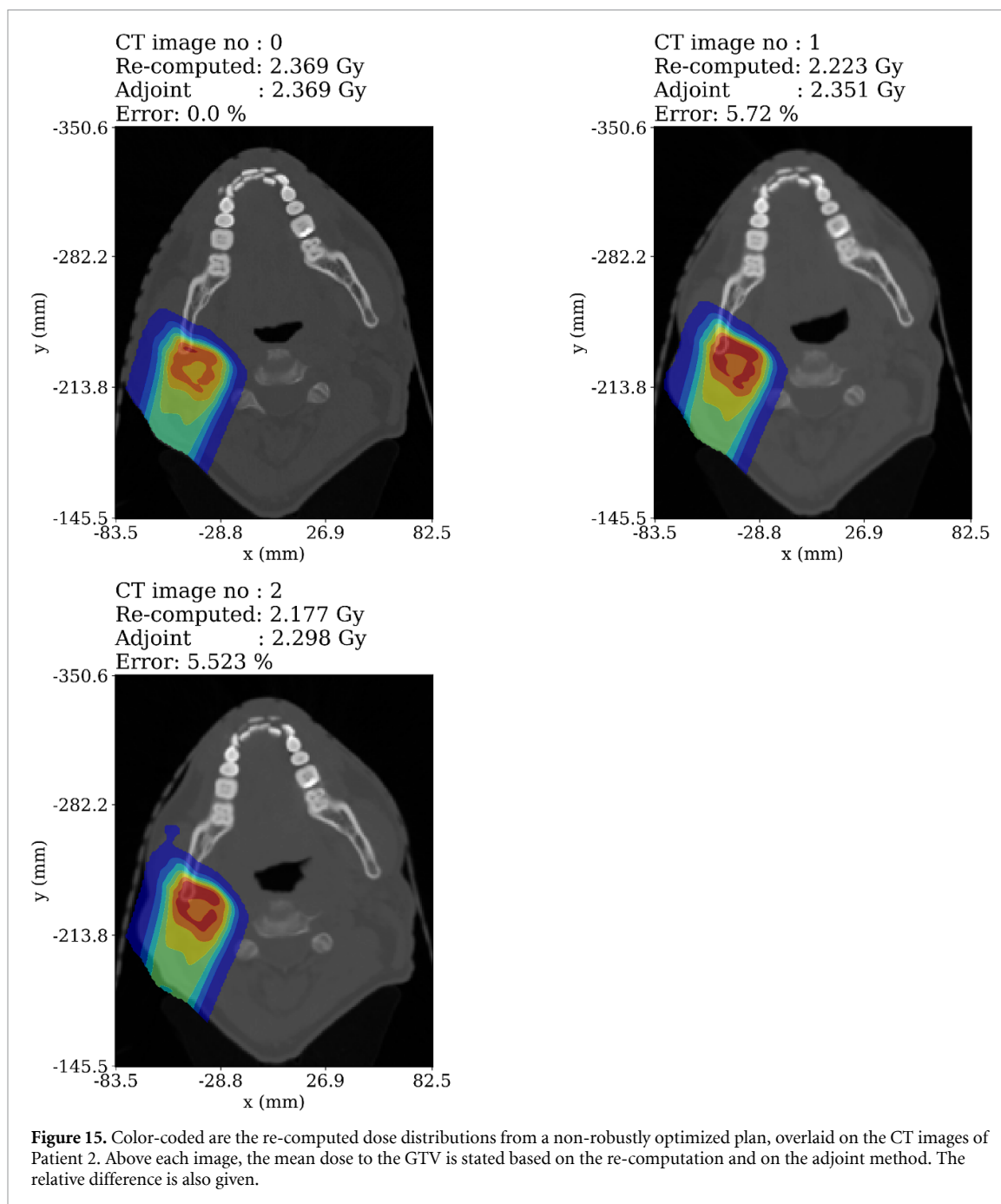


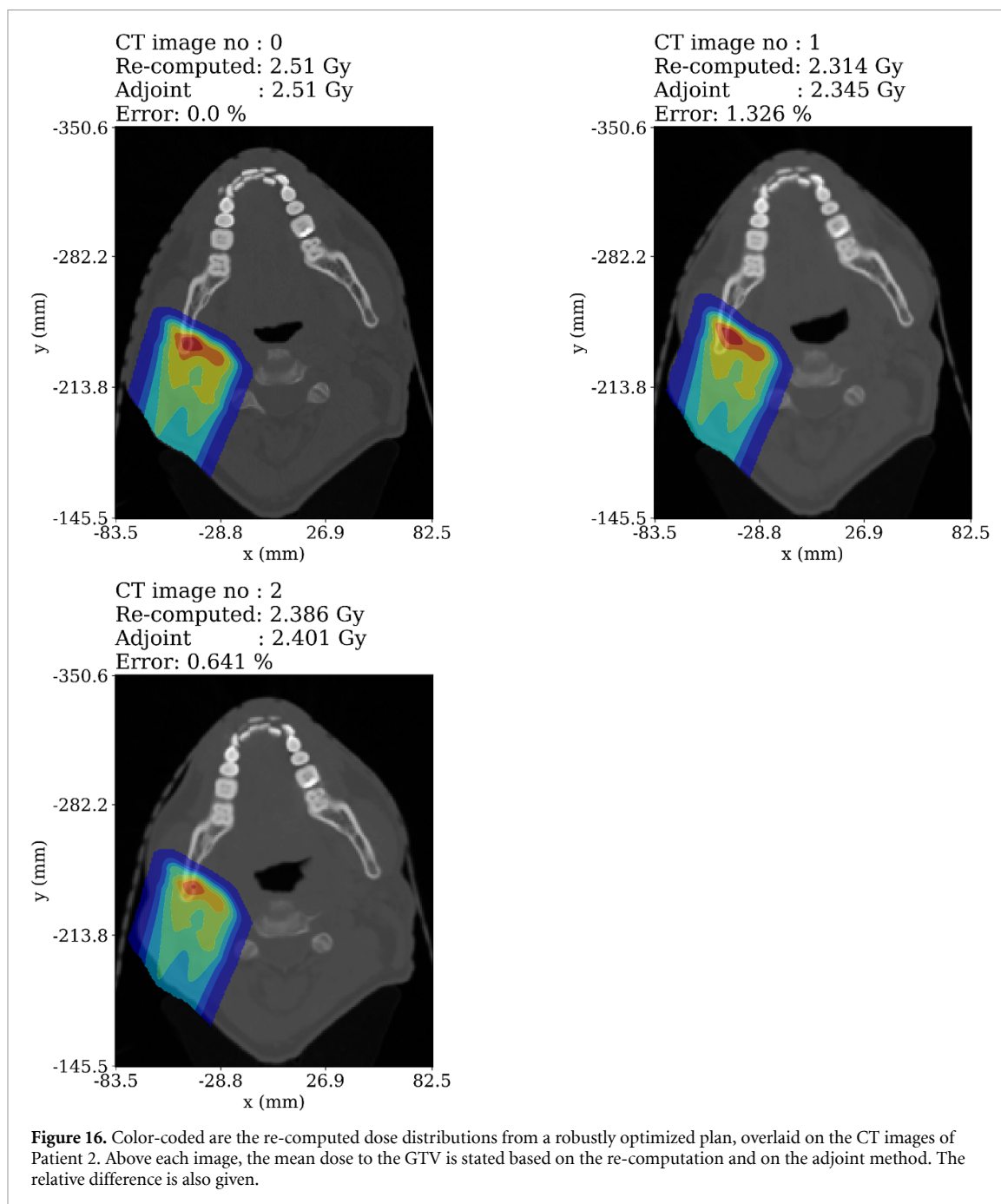
figure 13. In the case of the robustly optimized plan, the adjoint component attains a maximal error of 4.8%. Thus, whether the plan is robustly or non-robustly optimized, the adjoint component is capable of avoiding an expensive re-computation attaining an acceptable error.

Figures 15 and 16 shows each of the CT images for patient 2 (image number 0 is the planning image), a 2D dose slice of the re-computed dose distribution on the CT image, the GTV dose computed via re-computation and via the adjoint component and the relative error between these two results. In the case of the non-robustly optimized plan, the adjoint component attains a maximal error of 5.7% and in the case of the robustly optimized plan the adjoint component attains a maximal error of 1.3%. Here too the adjoint component computes the dose to the GTV with acceptable errors and is thus capable of avoiding expensive re-computations.



**Figure 14.** Color-coded are the re-computed dose distributions from a robustly optimized plan, overlaid on the CT images of Patient 1. Above each image, the mean dose to the GTV is stated based on the re-computation and on the adjoint method. The relative difference is also given.





## 4. Conclusions

In this work YODA and its performance in a variety of test cases was presented. YODA uses a hybrid approach to solve a physics-based approximation to the same equations that MC methods solve. This approach enables YODA to achieve TOPAS like performance with a significant speed-up. The lowest three dimensional gamma index passing rates achieved using the strict criteria of 1 mm, 1%, 10% cut-off is 94.55% in the Lung 2 case. YODA computes a treatment plan spot in 2 s while the same spot takes hours in TOPAS. An adjoint computation depends on the size of the structure but is generally in the order of milliseconds to tens of milliseconds on a single CPU. A typical commercial TPS plan re-evaluation is in the order of minutes to tens of minutes on multi-core CPUs or GPUs (Nystrom *et al* 2020). If YODA's speed would be further improved (e.g. via a GPU implementation), YODA could be used as a patient-specific quality assurance tool by tapping into the data stream between the TPS and the delivery machine to quickly re-construct the dose to be delivered. Alternatively, the logfiles could be used after treatment to re-construct the actually delivered dose to the patient. A multi-treatment site patient cohort study is necessary to validate the accuracy of YODA versus commercial TPS calculations in a wide variety of settings. Additionally, nuclear interactions must be accounted for. However, given that the dose engine contained in Eclipse (AcurosPT) is accurate with criteria of 2 mm, 2% in heterogeneous cases (De Martino *et al* 2021) and the various speed and accuracy improvements still achievable in YODA it can be concluded that this engine could compete with/replace other commercial dose algorithms and is certainly capable of TPS independent dose calculations.

Next to performing TPS independent dose calculations, YODA can leverage the adjoint component to accurately compute dose changes caused by small enough anatomical changes. Such a feature, to the best of the authors' knowledge, has not been integrated into a dose algorithm before. This component could be used in a time constrained re-adaptation trigger system where on the given day YODA avoids re-computing the old treatment plan on the new CT image if the CT image is deemed anatomically close enough to the original one. This performance was illustrated via four treatment plans where a maximal error of 5.7% was achieved for a non-robustly optimized plan and 4.8% for a robustly optimized plan. Alternatively, if log-files were available during treatment delivery YODA would be capable of halting erroneous deliveries in near real-time (i.e. below energy layer switching times) by converting spot position differences into anatomical changes and ultimately into dosimetric changes via the adjoint component.

## Data availability statement

The data cannot be made publicly available upon publication because they are owned by a third party and the terms of use prevent public distribution. The data that support the findings of this study are available upon reasonable request from the authors.

## Acknowledgments

The authors wish to acknowledge that the manuscript is partly funded by Varian, a Siemens Healthineers Company.

## Conflict of interest

The authors declare that they have no known competing financial interests or personal relationships that could have appeared to influence the work reported in this paper. Moreover, no data was used for the research described in the article.

## Credit statement

**Tiberiu Burlacu:** Conceptualization, methodology, software, validation, formal analysis, data curation, investigation, writing—original draft, writing—review & editing, visualization.

**Danny Lathouwers:** Conceptualization, methodology, software, validation, resources, writing—review & editing, supervision.

**Zoltán Perkó:** Conceptualization, methodology, validation, resources, writing—review & editing, supervision, project administration, funding acquisition.

## Appendix. Additional results

This appendix presents the results of the sliding slab experiment.

**Table 2.** Overview of the sliding slab experiment results. The table presents the beam energy, the slab HU value, the slab position with respect to the central beam axis, the used Gaussian splitting schemes, the gamma index settings and the gamma index pass rates.

Energy (MeV)	Slab value (HU)	Slab shift (mm)	Split scheme	Gamma settings (mm, %, %)	Gamma pass rate (%)
70	-1000	-4	1, 6, 6, 12	1, 1, 0	99.99
70	-1000	-4	1, 6, 6, 12	1, 1, 10	98.11
70	-1000	-4	1, 6, 6, 12, 12	1, 1, 0	99.99
70	-1000	-4	1, 6, 6, 12, 12	1, 1, 10	96.86
70	-1000	-4	1, 6, 6, 12, 12, 24	1, 1, 0	99.99
70	-1000	-4	1, 6, 6, 12, 12, 24	1, 1, 10	97.19
70	-1000	-2	1, 6, 6, 12	1, 1, 0	99.99
70	-1000	-2	1, 6, 6, 12	1, 1, 10	93.80
70	-1000	-2	1, 6, 6, 12, 12	1, 1, 0	99.99
70	-1000	-2	1, 6, 6, 12, 12	1, 1, 10	93.97
70	-1000	-2	1, 6, 6, 12, 12, 24	1, 1, 0	99.99
70	-1000	-2	1, 6, 6, 12, 12, 24	1, 1, 10	95.10
70	-1000	0	1, 6, 6, 12	1, 1, 0	99.99
70	-1000	0	1, 6, 6, 12	1, 1, 10	96.42
70	-1000	0	1, 6, 6, 12, 12	1, 1, 0	99.99
70	-1000	0	1, 6, 6, 12, 12	1, 1, 10	96.48
70	-1000	0	1, 6, 6, 12, 12, 24	1, 1, 0	99.99
70	-1000	0	1, 6, 6, 12, 12, 24	1, 1, 10	96.33
70	-1000	+2	1, 6, 6, 12	1, 1, 0	99.99
70	-1000	+2	1, 6, 6, 12	1, 1, 10	96.94
70	-1000	+2	1, 6, 6, 12, 12	1, 1, 0	99.99
70	-1000	+2	1, 6, 6, 12, 12	1, 1, 10	96.65
70	-1000	+2	1, 6, 6, 12, 12, 24	1, 1, 0	99.99
70	-1000	+2	1, 6, 6, 12, 12, 24	1, 1, 10	97.78
70	-1000	+4	1, 6, 6, 12	1, 1, 0	100.00
70	-1000	+4	1, 6, 6, 12	1, 1, 10	99.69
70	-1000	+4	1, 6, 6, 12, 12	1, 1, 0	99.99
70	-1000	+4	1, 6, 6, 12, 12	1, 1, 10	98.18
70	-1000	+4	1, 6, 6, 12, 12, 24	1, 1, 0	100.00
70	-1000	+4	1, 6, 6, 12, 12, 24	1, 1, 10	99.72

**Table 3.** Overview of the sliding slab experiment results. The table presents the beam energy, the slab HU value, the slab position with respect to the central beam axis, the used Gaussian splitting schemes, the gamma index settings and the gamma index pass rates.

Energy (MeV)	Slab value (HU)	Slab shift (mm)	Split scheme	Gamma settings (mm, %, %)	Gamma pass rate (%)
70	1000	-4	1, 6, 6, 12	1, 1, 0	100
70	1000	-4	1, 6, 6, 12	1, 1, 10	99.86
70	1000	-4	1, 6, 6, 12, 12	1, 1, 0	100
70	1000	-4	1, 6, 6, 12, 12	1, 1, 10	99.31
70	1000	-4	1, 6, 6, 12, 12, 24	1, 1, 0	100
70	1000	-4	1, 6, 6, 12, 12, 24	1, 1, 10	99.86
70	1000	-2	1, 6, 6, 12	1, 1, 0	99.99
70	1000	-2	1, 6, 6, 12	1, 1, 10	99.30
70	1000	-2	1, 6, 6, 12, 12	1, 1, 0	100
70	1000	-2	1, 6, 6, 12, 12	1, 1, 10	98.67
70	1000	-2	1, 6, 6, 12, 12, 24	1, 1, 0	100
70	1000	-2	1, 6, 6, 12, 12, 24	1, 1, 10	99.37
70	1000	0	1, 6, 6, 12	1, 1, 0	100
70	1000	0	1, 6, 6, 12	1, 1, 10	99.19
70	1000	0	1, 6, 6, 12, 12	1, 1, 0	100
70	1000	0	1, 6, 6, 12, 12	1, 1, 10	99.12
70	1000	0	1, 6, 6, 12, 12, 24	1, 1, 0	100
70	1000	0	1, 6, 6, 12, 12, 24	1, 1, 10	99.16
70	1000	+2	1, 6, 6, 12	1, 1, 0	99.99
70	1000	+2	1, 6, 6, 12	1, 1, 10	96.51
70	1000	+2	1, 6, 6, 12, 12	1, 1, 0	99.99
70	1000	+2	1, 6, 6, 12, 12	1, 1, 10	97.09
70	1000	+2	1, 6, 6, 12, 12, 24	1, 1, 0	100
70	1000	+2	1, 6, 6, 12, 12, 24	1, 1, 10	97.28
70	1000	+4	1, 6, 6, 12	1, 1, 0	99.99
70	1000	+4	1, 6, 6, 12	1, 1, 10	98.79
70	1000	+4	1, 6, 6, 12, 12	1, 1, 0	100
70	1000	+4	1, 6, 6, 12, 12	1, 1, 10	97.51
70	1000	+4	1, 6, 6, 12, 12, 24	1, 1, 0	100
70	1000	+4	1, 6, 6, 12, 12, 24	1, 1, 10	97.87

**Table 4.** Overview of the sliding slab experiment results. The table presents the beam energy, the slab HU value, the slab position with respect to the central beam axis, the used Gaussian splitting schemes, the gamma index settings and the gamma index pass rates.

Energy (MeV)	Slab value (HU)	Slab shift (mm)	Split scheme	Gamma settings (mm, %, %)	Gamma pass rate (%)
160	-1000	-4	1, 6, 6, 12	1, 1, 0	99.98
160	-1000	-4	1, 6, 6, 12	1, 1, 10	97.86
160	-1000	-4	1, 6, 6, 12, 12	1, 1, 0	99.95
160	-1000	-4	1, 6, 6, 12, 12	1, 1, 10	97.29
160	-1000	-4	1, 6, 6, 12, 12, 24	1, 1, 0	99.97
160	-1000	-4	1, 6, 6, 12, 12, 24	1, 1, 10	97.33
160	-1000	-2	1, 6, 6, 12	1, 1, 0	99.98
160	-1000	-2	1, 6, 6, 12	1, 1, 10	97.06
160	-1000	-2	1, 6, 6, 12, 12	1, 1, 0	99.97
160	-1000	-2	1, 6, 6, 12, 12	1, 1, 10	96.53
160	-1000	-2	1, 6, 6, 12, 12, 24	1, 1, 0	99.98
160	-1000	-2	1, 6, 6, 12, 12, 24	1, 1, 10	96.97
160	-1000	0	1, 6, 6, 12	1, 1, 0	99.98
160	-1000	0	1, 6, 6, 12	1, 1, 10	97.24
160	-1000	0	1, 6, 6, 12, 12	1, 1, 0	99.97
160	-1000	0	1, 6, 6, 12, 12	1, 1, 10	96.96
160	-1000	0	1, 6, 6, 12, 12, 24	1, 1, 0	99.97
160	-1000	0	1, 6, 6, 12, 12, 24	1, 1, 10	96.97
160	-1000	+2	1, 6, 6, 12	1, 1, 0	99.98
160	-1000	+2	1, 6, 6, 12	1, 1, 10	97.48
160	-1000	+2	1, 6, 6, 12, 12	1, 1, 0	99.98
160	-1000	+2	1, 6, 6, 12, 12	1, 1, 10	97.45
160	-1000	+2	1, 6, 6, 12, 12, 24	1, 1, 0	99.98
160	-1000	+2	1, 6, 6, 12, 12, 24	1, 1, 10	97.36
160	-1000	+4	1, 6, 6, 12	1, 1, 0	99.98
160	-1000	+4	1, 6, 6, 12	1, 1, 10	97.96
160	-1000	+4	1, 6, 6, 12, 12	1, 1, 0	99.98
160	-1000	+4	1, 6, 6, 12, 12	1, 1, 10	97.60
160	-1000	+4	1, 6, 6, 12, 12, 24	1, 1, 0	99.98
160	-1000	+4	1, 6, 6, 12, 12, 24	1, 1, 10	97.60

**Table 5.** Overview of the sliding slab experiment results. The table presents the beam energy, the slab HU value, the slab position with respect to the central beam axis, the used Gaussian splitting schemes, the gamma index settings and the gamma index pass rates.

Energy (MeV)	Slab value (HU)	Slab shift (mm)	Split scheme	Gamma settings (mm, %, %)	Gamma pass rate (%)
160	1000	-4	1, 6, 6, 12	1, 1, 0	99.99
160	1000	-4	1, 6, 6, 12	1, 1, 10	98.26
160	1000	-4	1, 6, 6, 12, 12	1, 1, 0	99.98
160	1000	-4	1, 6, 6, 12, 12	1, 1, 10	97.77
160	1000	-4	1, 6, 6, 12, 12, 24	1, 1, 0	99.98
160	1000	-4	1, 6, 6, 12, 12, 24	1, 1, 10	97.75
160	1000	-2	1, 6, 6, 12	1, 1, 0	99.98
160	1000	-2	1, 6, 6, 12	1, 1, 10	97.75
160	1000	-2	1, 6, 6, 12, 12	1, 1, 0	99.98
160	1000	-2	1, 6, 6, 12, 12	1, 1, 10	97.66
160	1000	-2	1, 6, 6, 12, 12, 24	1, 1, 0	99.98
160	1000	-2	1, 6, 6, 12, 12, 24	1, 1, 10	97.59
160	1000	0	1, 6, 6, 12	1, 1, 0	99.99
160	1000	0	1, 6, 6, 12	1, 1, 10	98.17
160	1000	0	1, 6, 6, 12, 12	1, 1, 0	99.98
160	1000	0	1, 6, 6, 12, 12	1, 1, 10	97.91
160	1000	0	1, 6, 6, 12, 12, 24	1, 1, 0	99.98
160	1000	0	1, 6, 6, 12, 12, 24	1, 1, 10	97.88
160	1000	+2	1, 6, 6, 12	1, 1, 0	99.99
160	1000	+2	1, 6, 6, 12	1, 1, 10	99.20
160	1000	+2	1, 6, 6, 12, 12	1, 1, 0	99.99
160	1000	+2	1, 6, 6, 12, 12	1, 1, 10	98.99
160	1000	+2	1, 6, 6, 12, 12, 24	1, 1, 0	99.99
160	1000	+2	1, 6, 6, 12, 12, 24	1, 1, 10	99
160	1000	+4	1, 6, 6, 12	1, 1, 0	99.99
160	1000	+4	1, 6, 6, 12	1, 1, 10	98.88
160	1000	+4	1, 6, 6, 12, 12	1, 1, 0	99.99
160	1000	+4	1, 6, 6, 12, 12	1, 1, 10	98.75
160	1000	+4	1, 6, 6, 12, 12, 24	1, 1, 0	99.99
160	1000	+4	1, 6, 6, 12, 12, 24	1, 1, 10	98.78

**Table 6.** Overview of the sliding slab experiment results. The table presents the beam energy, the slab HU value, the slab position with respect to the central beam axis, the used Gaussian splitting schemes, the gamma index settings and the gamma index pass rates.

Energy (MeV)	Slab value (HU)	Slab shift (mm)	Split scheme	Gamma settings (mm, %, %)	Gamma pass rate (%)
190	-1000	-4	1, 6, 6, 12	1, 1, 0	99.92
190	-1000	-4	1, 6, 6, 12	1, 1, 10	95.76
190	-1000	-4	1, 6, 6, 12, 12	1, 1, 0	99.86
190	-1000	-4	1, 6, 6, 12, 12	1, 1, 10	95.38
190	-1000	-4	1, 6, 6, 12, 12, 24	1, 1, 0	99.90
190	-1000	-4	1, 6, 6, 12, 12, 24	1, 1, 10	95.52
190	-1000	-2	1, 6, 6, 12	1, 1, 0	99.92
190	-1000	-2	1, 6, 6, 12	1, 1, 10	94.50
190	-1000	-2	1, 6, 6, 12, 12	1, 1, 0	99.91
190	-1000	-2	1, 6, 6, 12, 12	1, 1, 10	93.96
190	-1000	-2	1, 6, 6, 12, 12, 24	1, 1, 0	99.92
190	-1000	-2	1, 6, 6, 12, 12, 24	1, 1, 10	94.36
190	-1000	0	1, 6, 6, 12	1, 1, 0	99.93
190	-1000	0	1, 6, 6, 12	1, 1, 10	95.27
190	-1000	0	1, 6, 6, 12, 12	1, 1, 0	99.93
190	-1000	0	1, 6, 6, 12, 12	1, 1, 10	95.29
190	-1000	0	1, 6, 6, 12, 12, 24	1, 1, 0	99.93
190	-1000	0	1, 6, 6, 12, 12, 24	1, 1, 10	95.31
190	-1000	+2	1, 6, 6, 12	1, 1, 0	99.93
190	-1000	+2	1, 6, 6, 12	1, 1, 10	95.62
190	-1000	+2	1, 6, 6, 12, 12	1, 1, 0	99.93
190	-1000	+2	1, 6, 6, 12, 12	1, 1, 10	95.65
190	-1000	+2	1, 6, 6, 12, 12, 24	1, 1, 0	99.93
190	-1000	+2	1, 6, 6, 12, 12, 24	1, 1, 10	95.64
190	-1000	+4	1, 6, 6, 12	1, 1, 0	99.94
190	-1000	+4	1, 6, 6, 12	1, 1, 10	95.77
190	-1000	+4	1, 6, 6, 12, 12	1, 1, 0	99.94
190	-1000	+4	1, 6, 6, 12, 12	1, 1, 10	95.72
190	-1000	+4	1, 6, 6, 12, 12, 24	1, 1, 0	99.94
190	-1000	+4	1, 6, 6, 12, 12, 24	1, 1, 10	95.77

**Table 7.** Overview of the sliding slab experiment results. The table presents the beam energy, the slab HU value, the slab position with respect to the central beam axis, the used Gaussian splitting schemes, the gamma index settings and the gamma index pass rates.

Energy (MeV)	Slab value (HU)	Slab shift (mm)	Split scheme	Gamma settings (mm, %, %)	Gamma pass rate (%)
190	1000	-4	1, 6, 6, 12	1, 1, 0	99.95
190	1000	-4	1, 6, 6, 12	1, 1, 10	95.92
190	1000	-4	1, 6, 6, 12, 12	1, 1, 0	99.94
190	1000	-4	1, 6, 6, 12, 12	1, 1, 10	95.89
190	1000	-4	1, 6, 6, 12, 12, 24	1, 1, 0	99.94
190	1000	-4	1, 6, 6, 12, 12, 24	1, 1, 10	95.90
190	1000	-2	1, 6, 6, 12	1, 1, 0	99.94
190	1000	-2	1, 6, 6, 12	1, 1, 10	95.76
190	1000	-2	1, 6, 6, 12, 12	1, 1, 0	99.94
190	1000	-2	1, 6, 6, 12, 12	1, 1, 10	95.87
190	1000	-2	1, 6, 6, 12, 12, 24	1, 1, 0	99.94
190	1000	-2	1, 6, 6, 12, 12, 24	1, 1, 10	95.81
190	1000	0	1, 6, 6, 12	1, 1, 0	99.95
190	1000	0	1, 6, 6, 12	1, 1, 10	96.15
190	1000	0	1, 6, 6, 12, 12	1, 1, 0	99.95
190	1000	0	1, 6, 6, 12, 12	1, 1, 10	96.12
190	1000	0	1, 6, 6, 12, 12, 24	1, 1, 0	99.95
190	1000	0	1, 6, 6, 12, 12, 24	1, 1, 10	96.10
190	1000	+2	1, 6, 6, 12	1, 1, 0	99.96
190	1000	+2	1, 6, 6, 12	1, 1, 10	97.30
190	1000	+2	1, 6, 6, 12, 12	1, 1, 0	99.96
190	1000	+2	1, 6, 6, 12, 12	1, 1, 10	96.97
190	1000	+2	1, 6, 6, 12, 12, 24	1, 1, 0	99.96
190	1000	+2	1, 6, 6, 12, 12, 24	1, 1, 10	97.19
190	1000	+4	1, 6, 6, 12	1, 1, 0	99.96
190	1000	+4	1, 6, 6, 12	1, 1, 10	97.19
190	1000	+4	1, 6, 6, 12, 12	1, 1, 0	99.95
190	1000	+4	1, 6, 6, 12, 12	1, 1, 10	97.04
190	1000	+4	1, 6, 6, 12, 12, 24	1, 1, 0	99.96
190	1000	+4	1, 6, 6, 12, 12, 24	1, 1, 10	97.18

**Table 8.** Overview of the sliding slab experiment results. The table presents the beam energy, the slab HU value, the slab position with respect to the central beam axis, the used Gaussian splitting schemes, the gamma index settings and the gamma index pass rates.

Energy (MeV)	Slab value (HU)	Slab shift (mm)	Split scheme	Gamma settings (mm, %, %)	Gamma pass rate (%)
230	-1000	-4	1, 6, 6, 12	1, 1, 0	99.42
230	-1000	-4	1, 6, 6, 12	1, 1, 10	96.88
230	-1000	-4	1, 6, 6, 12, 12	1, 1, 0	99.13
230	-1000	-4	1, 6, 6, 12, 12	1, 1, 10	92.42
230	-1000	-4	1, 6, 6, 12, 12, 24	1, 1, 0	99.09
230	-1000	-4	1, 6, 6, 12, 12, 24	1, 1, 10	91.72
230	-1000	-2	1, 6, 6, 12	1, 1, 0	99.60
230	-1000	-2	1, 6, 6, 12	1, 1, 10	95.56
230	-1000	-2	1, 6, 6, 12, 12	1, 1, 0	99.32
230	-1000	-2	1, 6, 6, 12, 12	1, 1, 10	94.40
230	-1000	-2	1, 6, 6, 12, 12, 24	1, 1, 0	99.09
230	-1000	-2	1, 6, 6, 12, 12, 24	1, 1, 10	90.98
230	-1000	0	1, 6, 6, 12	1, 1, 0	99.65
230	-1000	0	1, 6, 6, 12	1, 1, 10	96.62
230	-1000	0	1, 6, 6, 12, 12	1, 1, 0	99.39
230	-1000	0	1, 6, 6, 12, 12	1, 1, 10	96.35
230	-1000	0	1, 6, 6, 12, 12, 24	1, 1, 0	99.15
230	-1000	0	1, 6, 6, 12, 12, 24	1, 1, 10	92.85
230	-1000	+2	1, 6, 6, 12	1, 1, 0	99.65
230	-1000	+2	1, 6, 6, 12	1, 1, 10	96.89
230	-1000	+2	1, 6, 6, 12, 12	1, 1, 0	99.40
230	-1000	+2	1, 6, 6, 12, 12	1, 1, 10	96.67
230	-1000	+2	1, 6, 6, 12, 12, 24	1, 1, 0	99.15
230	-1000	+2	1, 6, 6, 12, 12, 24	1, 1, 10	92.98
230	-1000	+4	1, 6, 6, 12	1, 1, 0	99.65
230	-1000	+4	1, 6, 6, 12	1, 1, 10	97.18
230	-1000	+4	1, 6, 6, 12, 12	1, 1, 0	99.41
230	-1000	+4	1, 6, 6, 12, 12	1, 1, 10	96.73
230	-1000	+4	1, 6, 6, 12, 12, 24	1, 1, 0	99.16
230	-1000	+4	1, 6, 6, 12, 12, 24	1, 1, 10	93.05

**Table 9.** Overview of the sliding slab experiment results. The table presents the beam energy, the slab HU value, the slab position with respect to the central beam axis, the used Gaussian splitting schemes, the gamma index settings and the gamma index pass rates.

Energy (MeV)	Slab value (HU)	Slab shift (mm)	Split scheme	Gamma settings (mm, %, %)	Gamma pass rate (%)
230	1000	−4	1, 6, 6, 12	1, 1, 0	99.65
230	1000	−4	1, 6, 6, 12	1, 1, 10	97.38
230	1000	−4	1, 6, 6, 12, 12	1, 1, 0	99.43
230	1000	−4	1, 6, 6, 12, 12	1, 1, 10	96.74
230	1000	−4	1, 6, 6, 12, 12, 24	1, 1, 0	99.19
230	1000	−4	1, 6, 6, 12, 12, 24	1, 1, 10	92.98
230	1000	−2	1, 6, 6, 12	1, 1, 0	99.64
230	1000	−2	1, 6, 6, 12	1, 1, 10	97.18
230	1000	−2	1, 6, 6, 12, 12	1, 1, 0	99.41
230	1000	−2	1, 6, 6, 12, 12	1, 1, 10	96.65
230	1000	−2	1, 6, 6, 12, 12, 24	1, 1, 0	99.17
230	1000	−2	1, 6, 6, 12, 12, 24	1, 1, 10	92.75
230	1000	0	1, 6, 6, 12	1, 1, 0	99.64
230	1000	0	1, 6, 6, 12	1, 1, 10	97.39
230	1000	0	1, 6, 6, 12, 12	1, 1, 0	99.40
230	1000	0	1, 6, 6, 12, 12	1, 1, 10	96.80
230	1000	0	1, 6, 6, 12, 12, 24	1, 1, 0	99.16
230	1000	0	1, 6, 6, 12, 12, 24	1, 1, 10	92.79
230	1000	+2	1, 6, 6, 12	1, 1, 0	99.61
230	1000	+2	1, 6, 6, 12	1, 1, 10	97.36
230	1000	+2	1, 6, 6, 12, 12	1, 1, 0	99.34
230	1000	+2	1, 6, 6, 12, 12	1, 1, 10	95.75
230	1000	+2	1, 6, 6, 12, 12, 24	1, 1, 0	99.10
230	1000	+2	1, 6, 6, 12, 12, 24	1, 1, 10	91.95
230	1000	+4	1, 6, 6, 12	1, 1, 0	99.61
230	1000	+4	1, 6, 6, 12	1, 1, 10	97.56
230	1000	+4	1, 6, 6, 12, 12	1, 1, 0	99.32
230	1000	+4	1, 6, 6, 12, 12	1, 1, 10	95.65
230	1000	+4	1, 6, 6, 12, 12, 24	1, 1, 0	99.08
230	1000	+4	1, 6, 6, 12, 12, 24	1, 1, 10	91.76

## ORCID iDs

Tiberiu Burlacu  <https://orcid.org/0000-0001-5542-6971>

Danny Lathouwers  <https://orcid.org/0000-0003-3810-1926>

Zoltán Perkó  <https://orcid.org/0000-0002-0975-4226>

## References

- Arjomandy B, Sahoo N, Zhu X R, Zullo J R, Wu R Y, Zhu M, Ding X, Martin C, Ciangaru G and Gillin M T 2009 An overview of the comprehensive proton therapy machine quality assurance procedures implemented at The University of Texas M. D. Anderson Cancer Center Proton Therapy Center–Houston *Med. Phys.* **36** 2269–82
- Barrett A, Morris S, Dobbs J and Roques T 2009 *Practical Radiotherapy Planning* (CRC Press)
- Beare R, Lowekamp B and Yaniv Z 2018 Image segmentation, registration and characterization in R with SimpleITK *J. Stat. Softw.* **86** 1–35
- Bodensteiner D 2018 RayStation: external beam treatment planning system *Med. Dosim.* **43** 168–76
- Bortfeld T 1997 An analytical approximation of the Bragg curve for therapeutic proton beams *Med. Phys.* **24** 2024–33
- Botas P, Kim J, Winey B and Paganetti H 2018 Online adaption approaches for intensity modulated proton therapy for head and neck patients based on cone beam CTs and Monte Carlo simulations *Phys. Med. Biol.* **64** 015004
- Burlacu T, Lathouwers D and Perkó Z 2023 A deterministic adjoint-based semi-analytical algorithm for fast response change computations in proton therapy *J. Comput. Theor. Transp.* **52** 1–41
- Craft D, Bangert M, Long T, Papp D and Unkelbach J 2014 Supporting material for: ‘Shared data for IMRT optimization research: the CORT dataset’ (<https://doi.org/10.5524/100110>)
- De Martino F, Clemente S, Graeff C, Palma G and Cella L 2021 Dose calculation algorithms for external radiation therapy: an overview for practitioners *Appl. Sci.* **11** 6806
- der Voort S V, van de Water S, Perkó Z, Heijmen B, Lathouwers D and Hoogeman M 2016 Robustness recipes for minimax robust optimization in intensity modulated proton therapy for oropharyngeal cancer patients *Int. J. Radiat. Oncol. Biol. Phys.* **95** 163–70
- Eyges L 1948 Multiple scattering with energy loss *Phys. Rev.* **74** 1534–5

- Frank S J and Zhu X R 2020 *Proton Therapy Indications, Techniques and Outcomes* (Elsevier Inc.) (<https://doi.org/10.1016/C2019-0-00724-8>)
- Gebäck T and Asadzadeh M 2012 Analytical solutions for the pencil-beam equation with energy loss and straggling *Transp. Theory Stat. Phys.* **41** 325–36
- Gerbershagen A, Adelmann A, Dölling R, Meer D, Rizzoglio V and Schippers J 2017 Simulations and measurements of proton beam energy spectrum after energy degradation *J. Phys.: Conf. Ser.* **874** 012108
- Gottschalk B 2004 *Passive Beam Spreading in Proton Radiation Therapy* draft edn (Harvard High Energy Physics Laboratory)
- Gottschalk B 2012 Techniques of proton radiotherapy: transport theory (arXiv:1204.4470 [physics.med-ph])
- Johnson J E, Beltran C, Wan Chan Tseung H, Mundy D W, Kruse J J, Whitaker T J, Herman M G and Furutani K M 2019 Highly efficient and sensitive patient-specific quality assurance for spot-scanned proton therapy *PLoS One* **14** e0212412
- Kennedy C A and Carpenter M H 2016 *Diagonally Implicit Runge-Kutta Methods for Ordinary Differential Equations. A Review* NASA/TM-2016-219173 (NASA Langley Research Center Hampton, VA, United States) (available at: <https://ntrs.nasa.gov/citations/20160005923>)
- Lalee M, Necedal J and Plantenga T 1998 On the implementation of an algorithm for large-scale equality constrained optimization *SIAM J. Optim.* **8** 682–706
- Li H, Sahoo N, Poenisch F, Suzuki K, Li Y, Li X, Zhang X, Lee A K, Gillin M T and Zhu X R 2013 Use of treatment log files in spot scanning proton therapy as part of patient-specific quality assurance *Med. Phys.* **40** 021703
- Lomax A J 2008a Intensity modulated proton therapy and its sensitivity to treatment uncertainties 1: the potential effects of calculational uncertainties *Phys. Med. Biol.* **53** 1027–42
- Lomax A J 2008b Intensity modulated proton therapy and its sensitivity to treatment uncertainties 2: the potential effects of inter-fraction and inter-field motions *Phys. Med. Biol.* **53** 1043–56
- Meier G, Besson R, Nanz A, Safai S and Lomax A J 2015 Independent dose calculations for commissioning, quality assurance and dose reconstruction of PBS proton therapy *Phys. Med. Biol.* **60** 2819–36
- Meijers A, Guterres Marmitt G, Ng Wei Siang K, van der Schaaf A, Knopf A C, Langendijk J A and Both S 2020 Feasibility of patient specific quality assurance for proton therapy based on independent dose calculation and predicted outcomes *Radiother. Oncol.* **150** 136–41
- Men C, Jia X and Jiang S B 2010 GPU-based ultra-fast direct aperture optimization for online adaptive radiation therapy *Phys. Med. Biol.* **55** 4309–19
- Nystrom H, Jensen M F and Nystrom P W 2020 Treatment planning for proton therapy: what is needed in the next 10 years? *Br. J. Radiol.* **93** 20190304
- Paganetti H (ed) 2016 *Proton Therapy Physics* (CRC Press)
- Paganetti H, Botas P, Sharp G C and Winey B 2021 Adaptive proton therapy *Phys. Med. Biol.* **66** 22TR01
- Pastor Serrano O 2023 Artificial intelligence in radiotherapy: probabilistic deep learning for dose prediction and anatomy modeling *Doctoral Thesis* (<https://doi.org/10.4233/uuid:c0c501d2-7c05-4e95-b8e8-d81aab627bb9>)
- Perl J, Shin J, Schumann J, Faddegon B and Paganetti H 2012 TOPAS: an innovative proton Monte Carlo platform for research and clinical applications *Med. Phys.* **39** 6818–37
- Pomraning G C 1996 Higher order Fokker-Planck operators *Nucl. Sci. Eng.* **124** 390–7
- Pomraning G C and Prinja A K 1999 A large deflection Fermi–Eyges pencil beam formula *Ann. Nucl. Energy* **26** 595–609
- Rivière B 2008 *Discontinuous Galerkin Methods for Solving Elliptic and Parabolic Equations (Frontiers in Applied Mathematics)* (Society for Industrial and Applied Mathematics)
- Scott W T 1963 The theory of small-angle multiple scattering of fast charged particles *Rev. Mod. Phys.* **35** 231–313
- Soukup M, Fippel M and Alber M 2005 A pencil beam algorithm for intensity modulated proton therapy derived from Monte Carlo simulations *Phys. Med. Biol.* **50** 5089–104
- Trnková P, Bolsi A, Albertini F, Weber D C and Lomax A J 2016 Factors influencing the performance of patient specific quality assurance for pencil beam scanning IMPT fields *Med. Phys.* **43** 5998–6008
- Unkelbach J and Paganetti H 2018 Robust proton treatment planning: physical and biological optimization *Semin. Radiat. Oncol.* **28** 88–96
- Van de Water S, van Dam I, Schaart D R, Al-Mamgani A, Heijmen B J M and Hoogeman M S 2016 The price of robustness; impact of worst-case optimization on organ-at-risk dose and complication probability in intensity-modulated proton therapy for oropharyngeal cancer patients *Radiother. Oncol.* **120** 56–62
- Virtanen P et al 2020 SciPy 1.0: fundamental algorithms for scientific computing in Python *Nat. Methods* **17** 261–72
- Yang J, He P, Wang H, Sun G, Zheng H and Jia J 2020 An improved beam splitting method for intensity modulated proton therapy *Phys. Med. Biol.* **65** 185015
- Yorke A A, McDonald G C, Solis D and Guerrero T 2019 Pelvic reference data (<https://doi.org/10.7937/TCIA.2019.WOSKQ5000>)
- Zheng-Ming L and Brahme A 1993 An overview of the transport theory of charged particles *Radiat. Phys. Chem.* **41** 673–703